On the impact of ice formation processes and sedimentation on cirrus origin classification in WCB outflow

Tim Lüttmer[1], Annette Miltenberger[1], and Peter Spichtinger[1]

[1]Institute for Atmospheric Physics, Johannes Gutenberg University Mainz, Mainz, Germany

Correspondence: Tim Lüttmer (tluettm@uni-mainz.de)

Abstract. Formation pathways of cirrus clouds are thought to differ in the dominant ice nucleation mechanism and the thermodynamic regime: liquid origin cirrus are forming at water saturation and ice crystals from by freezing of liquid water drops, while in-situ cirrus form below water saturation at low temperatures ($T < 235\,\mathrm{K}$) and ice crystals form without an intermediate, stable liquid phase.

Warm conveyor belts (WCBs) can transport liquid droplets as well as vapor from the boundary layer into the upper troposphere, where cirrus is formed in the outflow. The dominant ice formation pathway remains uncertain. We employ a two-moment multi-class cloud microphysics scheme that distinguish between five ice classes. Each ice class represents ice formed by a unique formation mechanism. Thus, the formation signature is available even a long time after the formation process.

Our analysis for a WCB case study shows that cirrus in its WCB outflow consist predominantly of ice formed by processes only active below water saturation. Hence suggesting in-situ origin from a nucleation perspective. However, Lagrangian trajectories show that the cirrus is derived from mixed-phase clouds suggesting liquid origin from a thermodynamic perspective. We found that sedimentation is a key process for the vertical redistribution of ice formed by different pathways. The main WCB ascent region was embedded in a slow ascending air mass that resulted in in-situ ice formation above the WCB. This in-situ formed ice sedimented into mixed-phase clouds of the WCB below, which also altered macrophysical properties of the outflow cirrus.

1 Introduction

One of the major cloud producing synoptic-scale phenomena in the extra-tropical atmosphere are the so-called warm-conveyor belts (WCB), which are coherent air streams that transport moist air masses from the planetary boundary layer to the upper troposphere. WCBs originate from the warm sector of extratropical cyclones and occur frequently in the Northern Hemisphere during all seasons (Madonna et al., 2014). They form long cloud bands during ascend, consisting of pure water, mixed-phase and pure ice clouds. In the outflow region of the WCB vast fields of high altitude, pure ice clouds (cirrus) are formed.

WCBs affect the weather evolution and climate state in several ways. A large part of total and extreme precipitation in many parts of the extratropics can be attributed to WCBs (Pfahl et al., 2014; Joos et al., 2023). Latent heat released from cloud microphysics processes occurring in the WCB cloud band causes diabatic modification of Potential Vorticity (PV) (Wernli and Gray, 2024). These PV anomalies influence the upper-level flow downstream of the WCB (Grams et al., 2011; Rodwell et al., 2018; Grams et al., 2018) and affect cyclone development by increasing their intensification rate (Reed et al., 1992; Binder

et al., 2016).

The cloud fields of the WCB also influence cloud radiative effect (CRE) in the extratropics (Joos, 2019). CRE and changes thereof are an important component for determining the climate state, but may also impact the thermodynamic structure of the extra-tropical tropopause region, upper-tropospheric flow, and exchange between tropopshere and stratosphere (see, e.g., Hong et al., 2016; Matus and L'Ecuyer, 2017; Spreitzer et al., 2019). The sign of cloud radiative effect (CRE) is determined by the net of two opposing effects (Ramanathan et al., 1989). The albedo effect describes the ability of clouds to (partly) scatter and reflect incoming solar radiation back to space, leading to a cooling effect on the Earth's surface temperature. The greenhouse effect describes the ability of clouds to (partly) absorb and re-emit terrestrial radiation towards the Earth's surface, hence warming it. For stratiform cirrus clouds the sign of the net radiative effect is uncertain and depends on the bulk properties of the cirrus cloud (Zhang et al., 1999; Krämer et al., 2020). High Ice Water Content (IWC) and large mean diameters of ice crystals result in a positive (warming) CRE, whereas small mean diameters and low IWC result in a negative (cooling) CRE (Zhang et al., 1999). These bulk properties of cirrus cloud depend on their formation pathway (Krämer et al., 2016; Luebke et al., 2016; Wolf et al., 2018; Krämer et al., 2020). Of course, CRE also depends on other components of the Earth-atmosphere system, e.g., surface albedo and coverage of lower level clouds.

In general we distinguish between two formation pathways of cirrus clouds (see, e.g., Krämer et al., 2016; Wernli et al., 2016): (i) liquid-origin and (ii) in-situ cirrus. Liquid-origin cirrus (i) ice crystals are created by freezing of pre-existing water droplets. This requires the ascent in a mixed-phase cloud that extends to low temperatures to attain complete glaciation and produce cirrus. The ascent can be slow and gradual, e.g. as part of a warm conveyor belt, or fast, driven by (embedded) convection. Freezing of (pure) water droplets can be induced by aerosols that show ice nucleating (surface) properties, which are referred to as ice nucleating particles (INP). Here we can distinguish between the immersion and contact freezing modes (Vali et al., 2015). In the absence of active INPs, droplets will freeze homogeneously, particularly close to the homogeneous freezing temperature threshold ($T_c = 235\,\mathrm{K}$). The liquid origin ice formation pathway occurs close to water saturation since (pure) water droplets would otherwise evaporate. In the other possible cirrus formation pathway, i.e. in-situ cirrus (ii), ice crystals are directly formed from water vapor and (liquid or solid) aerosols without them being first activated to cloud droplets. Hence, this formation pathway occurs at lower temperatures and below water saturation. In subsaturated conditions with respect to liquid water, new ice crystals can be formed by deposition of water vapour onto a (solid) INP like dust, soot or biological aerosols (deposition nucleation) or by freezing of aqueous solution droplets (homogeneous nucleation).

Previous studies have suggested, that the different thermodynamic pathway and ice formation processes result in different bulk properties of the cirrus: Liquid origin cirrus are thought to be 'thicker' than in-situ cirrus, i.e. they are associated with high IWC and larger ice crystals diameters (see, e.g., Luebke et al., 2016; Wolf et al., 2018). These studies also suggested that liquid origin cirrus clouds likely consist of much more ice particles than in-situ formed cirrus clouds. While in-situ cirrus are typically optically thinner than liquid origin cirrus, two subcategories of in-situ cirrus with vastly different microphysical and radiative properties can be identified: Cirrus forming in slow updrafts ($<10\,\mathrm{cm\,s^{-1}}$) are characterized by few large crystals from deposition nucleation. These clouds show a small net warming effect (Krämer et al., 2020). In contrast, in-situ cirrus formed in fast updrafts is associated with homogeneous freezing of small liquid aerosols resulting in many small ice crystals. These cirrus

either have a small net warming or a net cooling effect depending on their altitude (Joos et al., 2014; Krämer et al., 2020).

Quantifying and understanding characteristic differences between cirrus formed via different pathways is contingent on a robust classification of observed or modelled cirrus clouds. In the past decade several approaches have been proposed, which largely rely on the investigation of airmass trajectories from models, cloud temperature or indeed the cloud properties themselves.

Lagrangian based methods are used to identify formation pathways of cirrus in model simulations. Wernli et al. (2016) developed an algorithm that investigated backward trajectories originating from cirrus clouds until the air parcel contained no ice. If the segment contained any liquid water content (LWC), the cirrus cloud was classified as liquid origin otherwise it was classified as in-situ. Wernli et al. (2016) applied this classification to 12 years of ERA-interim data for the North Atlantic storm track region. They found that the occurrence frequency of cloud types strongly varies with altitude with liquid origin cirrus typically found at lower altitudes. Also their analysis suggests that more than $80\,\%$ of liquid origin cirrus clouds are topped with an in-situ cloud.

Difference in cirrus cloud properties due to the formation pathway can be identified by combining Lagrangian information about the thermodynamic history with observational data on ice crystal properties (which are not well represented in model and reanalysis data). Luebke et al. (2016) used airborne, in-situ measurements of IWC, cloud ice numbers concentration (n_i) and ice crystal size (D_i) to demonstrate the differences between liquid origin and in-situ formed cirrus. Wolf et al. (2018) used balloon-borne, in-situ observations to investigate ice crystal size distributions in Arctic cirrus clouds. Both studies utilized the CLaMS-Ice microphysics model (Spichtinger and Gierens, 2009) to simulate the cirrus cloud development. CLaMS-Ice was run along Lagrangian backward trajectories. ECMWF operational analysis data was used to drive the trajectory model. The observed cloud was classified as in-situ if cloud ice did (first) appear below the homogeneous freezing threshold (or cirrus temperature level) ($T_c = 235\,\mathrm{K}$). Below T_c water and ice phase cannot coexist, thus the ice formation has to be in-situ. The cloud was classified as liquid origin if the temperature at the first occurrence of cloud ice was above T_c and the measurement was taken at pressure levels more than $500\,\mathrm{hPa}$.

A temperature based classification of cirrus clouds can also be used without employing Lagrangian trajectories. Gasparini et al. (2018) compared cloud patterns from global simulations of the ECHAM-HAM general circulation model to CALIPSO satellite data. As in Luebke et al. (2016) they used a temperature based criterion to distinguish between liquid origin and in-situ cirrus. Ice clouds which cloud bases extended to $238\,\mathrm{K}$ were classified as liquid origin and all other cirrus clouds as in-situ.

Another method for cirrus origin classification not relying on Lagrangian information is to utilize retrievals from remote sensing to estimate cirrus properties and then search for signatures that match the characteristics of the cloud types. Huo et al. (2020) utilized 4 years of ground based radar measurements in Beijing to obtain cloud properties. They classified the cirrus origin by cloud temperature and reflectivity to match proposed cloud properties of previous studies (e.g. Krämer et al., 2016; Luebke et al., 2016). Urbanek et al. (2017) used backscatter ratio lidar from atmospheric cross sections to identify in-cloud and cloud-free regions. With ice supersaturation (S_i) from synergistic lidar measurements and temperature fields derived from ECMWF model data, they determined the cloud type by application of S_i threshold values. Observations processed from satellites (e.g., CALIPSO and CloudSat) provide multiple years of statistics of cirrus cloud properties (Sourdeval et al., 2018;

Gryspeerdt et al., 2018). That data was used to derive a global climatology of ice concentrations n_i based on the agreement between remote sensing and in-situ measurements (Krämer et al., 2020). The data of n_i coupled with cloud temperatures gave indications of the cirrus origin.

These approaches have their limitations. For classification with observations, measured cloud properties are compared with characteristic values of the cloud type. However, remote sensing methods do not report on the history of the cloud and cloud processes like ice crystal growth, aggregation and sedimentation. Therefore, classification methods only based on instantaneous data can not distinguish to what degree observed cloud properties are characteristic for the formation process and to what degree they were distorted by other cloud processes (Krämer et al., 2020). Further, a temperature based classification can misidentify the cloud type when the horizontal dimension of the cloud is not considered (Gasparini and Lohmann, 2016). Lagrangian methods are subject to uncertainties as well, which arise due to uncertainties in the underlying wind field data or an inadequate representation of convection and meso-scale temperature fluctuations. Simulations at high resolution can help mitigating some of these issues (Wernli et al., 2016). Running a parcel microphysics model like CLaMS-Ice along the trajectory path to investigate the cloud history may improve the representation of ice cloud physics, but typically there is no or very limited feedback of the ensuing diabatic processes on the vertical velocity and thermodynamic evolution of the parcel itself and in most parcel models sedimentation of cloud ice from other regions into parcel is not considered. Therefore trajectory-based classification can be 'confused' if cloud ice from different formation pathways mixes through sedimentation and turbulence thus altering the cloud properties (Wernli et al., 2016).

In this study we utilise a recently developed ice modes microphysics scheme (Lüttmer et al., 2024) that retains information about the ice formation mechanism throughout Eulerian simulations of cloud evolution to investigate ice formation mechanism in WCB related cirrus clouds and their impact on the cirrus properties. The simulation and analysis is conducted for a WCB occurring between 3rd and 6th October 2016 in the North Atlantic and was investigated from a dynamical point of view in earlier studies by Oertel et al. (2023). The ice modes scheme introduces multiple ice classes ('ice modes') in a two-moment microphysics scheme that are each unique by their formation process. In Lüttmer et al. (2024) we employed the ice modes scheme to investigate ice formation in an idealized deep convection case. Consistent with expectations we found that the convective ice clouds were of liquid origin with traces of ice stemming from in-situ formation in the overshoot. In this study we employ the same microphysics scheme for a WCB case using high-resolution simulations with the ICON atmospheric model. Thereby we circumvent one key disadvantages of Lagrangican cirrus classification, as the new model allows for a proper representation of sedimentation effects.

In Section 2 we describe the model set-up, including a brief introduction of the ice modes microphysics scheme, the employed cirrus classification algorithms and observational data used. In Section 3 we introduce the case study and investigate the contribution of different ice modes to the mixed-phase and cirrus clouds associated with the WCB air stream. In Section 4 we present an analysis of liquid origin and in-situ cirrus properties. Results for classifications based on information from the ice mode scheme and information on the thermodynamic history (i.e. according to Wernli et al., 2016) are compared and discussed. Finally, the key findings are summarised in Section 5 and implications for future work are discussed.

2 Methods

For our investigation of the physical link between ice formation mechanisms, thermodynamic cirrus formation pathways, and cirrus properties we choose a cyclone that occurred during the NAWDEX campaign between the 3th and 6th October 2016 over the North Atlantic (Schäfler et al., 2018). This case has been studied in previous literature with a focus on diabatic flow modifications (Oertel et al., 2023).

2.1 Model setup

Simulations of the meteorological evolution over the North Atlantic during the selected time period are conducted with the Icosahedral Nonhydrostatic Weather and Climate Model (ICON) version 2.6. The ICON configuration follows largely Heinze et al. (2017) in a limited area mode and additionally employs the ice modes scheme (Lüttmer et al., 2024). We use a R03B08 model grid with an effective horizontal resolution of $6.5\,\mathrm{km}$ and vertical grid with 90 levels in a terrain-following coordinate system (SLEVE). The model domain extends from $70°\,\mathrm{W}$ to $50°\,\mathrm{E}$ and $20°\,\mathrm{N}$ to $80°\,\mathrm{N}$, respectively. The domain thus includes most of the Northern Atlantic and Europe. The model is integrated with a physics time step of $40\,\mathrm{s}$. Initialisation and boundary data is provided by ECMWF Integrated Forecasting System (IFS) reanalysis data (Bechtold et al., 2008). The simulation is started on 4th October 2016 00 UTC and is run for $54\,\mathrm{h}$ including a $6\,\mathrm{h}$ spin-up phase. Model output is written every $30\,\mathrm{min}$ and interpolated from the icosahedral model grid to a latitude-longitude grid ($0.075°\,\mathrm{x}0.075°$). This interpolated data is used for all analysis in our study.

We include most of the physics parameterisations commonly used in ICON: TERRA surface model (Heise et al., 2016), surface transfer scheme (Louis, 1979), subgrid scale orographic drag (Lott and Miller, 1997), non-orographic gravity wave drag (Orr et al., 2010), vertical diffusion and transfer by turbulence (Raschendorfer, 2001), and a radiation transfer model (Mlawer et al., 1997) in conjunction with a simple cloud cover parametrisation. Further discussions regarding these configuration can be found in Heinze et al. (2017). We do neither use a deep nor shallow convection scheme, as the assumptions and implementation are not compatible with the used cloud microphysics scheme and in particular its ice modes extension (see Lüttmer et al. (2024) and Section 2.2).

2.2 Ice modes scheme

The simulations employ the ice mode schemes, which is a derivation of the two-moment microphyiscs parametrisation in ICON (Seifert and Beheng, 2006). The scheme expands the "standard" two-moment scheme by introducing additional hydrometeor classes, i.e. in addition to cloud droplets, raindrops, snow, graupel and hail, there are five ice classes (subsequently called "ice modes") each with their distinct formation pathway and which are described by the following additional prognostic variables:

- **HOM ice mode** (n_{hom}, q_{hom}): Ice crystals formed by homogeneous freezing of solution droplets
- **FRZ ice mode** (n_{frz}, q_{frz}): Ice crystals formed by homogeneous freezing of cloud droplets
- **IMM ice mode** (n_{imm}, q_{imm}): Ice crystals formed by immersion freezing of cloud and rain droplets
- **DEP ice mode** (n_{dep}, q_{dep}): Ice crystals formed by deposition nucleation

– **SEC ice mode** (n_{sec}, q_{sec}): Ice crystals formed by secondary ice formation processes

Additionally we refer to TOT as the sum of all ice modes, representing all cloud ice

$$q_{tot} = q_{hom} + q_{frz} + q_{imm} + q_{dep} + q_{sec} \qquad\qquad n_{tot} = n_{hom} + n_{frz} + n_{imm} + n_{dep} + n_{sec} \qquad (1)$$

Note that TOT is a diagnostic property and not a distinct ice mode in the model.

At each grid point multiple unique ice formation processes can be active within a time step, providing ice to their associated ice modes. Ice modes can coexist and each ice mode is described by its own size distribution. The type of all size distributions is a generalized gamma distribution and represented in the model by two prognostic moments, i.e. the number n_x and mass densities q_x. The shape of an ice crystals mainly depends on temperature and supersaturation, which controls the growth behavior of the crystal by deposition of vapor. Therefore we assume the same shape, mass-diameter and fallspeed relations for each ice mode. They are also treated equally in advection, depositional growth and can collide with each particle class including itself and other ice modes. Note that aggregation of any ice mode contributes only to the same snow class.

The following paramterisations are used for primary and secondary ice formation processes our ICON configuration. Homogeneous freezing of solution droplets (contributing to HOM) is described by the parametrisation of Kärcher and Lohmann (2002). For homogeneous freezing of cloud droplets (contributing to FRZ) the fit of Cotton and Field (2002) is used. Immersion freezing of raindrops (contributing to IMM) is represented by the parametrisation of Bigg (1953). Heterogeneous nucleation of ice contributes both to the IMM and DEP ice mode and is governed by the number concentration, size distribution and activation scheme of ice nucleating particles (INP). In this study we use the parametrisation of Hande et al. (2015) for dust events over Europe. Here deposition nucleation can only occur outside of mixed-phase clouds ($q_c + q_{cr} = 0$). The only secondary ice mechanisms considered in the present study is rime splintering (Hallett-Mossop process).

A detailed description of the ice modes scheme can be found in Lüttmer et al. (2024).

2.3 WCB trajectories

The main synoptic-scale cloud producing feature in our case study is an extratropical cyclone and the associated WCB. In order to investigate the impact of this system on cirrus formation we identify its position and spatio-temporal evolution by airmass trajectories calculated offline from the ICON half-hourly windfield data with the LAGRANTO software (Sprenger and Wernli, 2015). The gridded model data is interpolated onto the positions of the airmass trajectories at each output interval. The output interval of LAGRANTO is chosen such that it aligns with the output interval of the ICON model simulations.

Trajectories are started $6\,\mathrm{h}$ after model initialisation at 4th October 2016 06:00 UTC in a large box around the cyclone from $50°\,\mathrm{W}$ to $20°\,\mathrm{W}$ and $30°\,\mathrm{N}$ to $65°\,\mathrm{N}$. Trajectories are started from a $7.5\,\mathrm{km}$ equidistant horizontal grid grid and at five altitude levels from the surface up to $1\,\mathrm{km}$.

Trajectories constituting the WCB are identified by two conditions (Joos and Wernli, 2012; Madonna et al., 2014): First they have to ascend at least $600\,\mathrm{hPahPa}$ in $48\,\mathrm{h}$. Second they need to start in or cross a cyclone. Cyclones are identified with a newly developed algorithm as two dimensional features in the surface pressure field based on Wernli and Schwierz (2006) (see Appendix B). The newly developed algorithm contains a different approach for calculation of the cyclone contours. We also

195   added new selection criterion for identifying cyclones.

After selecting WCB trajectories we calculate an WCB area index marking the grid cell and model level where a WCB trajectory is present for each time step. This allows to investigate the evolution of (micro-)physical quantities both interpolated on the trajectories as well as in the gridded model data itself.

To characterize the flow and clouds above the WCB additional trajectories were started hourly in large region around the WCB
200   from $50°\,\mathrm{W}$ to $30°\,\mathrm{E}$ and $32.5°\,\mathrm{N}$ to $75°\,\mathrm{N}$ starting at 8 altitude levels between approximately $7\,\mathrm{km}$ up to the tropopause. This results in on average 15000 trajectories starting per hour. These trajectories are computed backwards in time until the start date of the simulation. Using the WCB area index we selected all trajectories that passed above but did not intersect vertically with the WCB and stayed above $5\,\mathrm{km}$ at all times. The remaining trajectory data-sets characterises the airflow in the upper-troposphere above the WCB and excludes strongly ascending trajectories, which are part of the WCB itself.

205 **2.4   Cirrus cloud origin classification**

In-line with the objective of our study to understand the impact of different ice formation mechanisms for cirrus properties, we follow the cirrus classification approach by Krämer et al. (2016) in combination with the novel ice modes scheme: Liquid origin cirrus are formed from freezing droplets that were transported into the cirrus temperature region ($T < T_c = 235\,\mathrm{K}$). Thus it originates from liquid or mixed-phase clouds. Ice crystals in the homogeneous (FRZ) and immersion freezing (IMM) ice
210   modes are classified as liquid origin cirrus (if present at sufficiently low temperatures). In-situ cirrus is formed directly as ice from the vapor phase onto the surface of ice nucleating particles (INPs). The homogeneous nucleation (HOM) and deposition nucleation (DEP) ice modes contribute to in-situ ice.

Each grid point in the model likely contains a mixture of different ice modes, therefore we define the liquid origin fraction f_{liq} as the ratio of cloud ice content of liquid origin to the total cloud ice content:

215
$$f_{liq} = \frac{q_{frz} + q_{imm}}{q_{frz} + q_{imm} + q_{hom} + q_{dep}} \tag{2}$$

This allows a comprehensive description of the cirrus origin for grid-point data. f_{liq} can change each time step as cloud processes, most notably sedimentation and ice nucleation, modify the prognostic moments of the ice modes at each grid-point. Note that we did not include the SEC mode since secondary ice can not inherently be associated with either in-situ or liquid origin formation pathway. However, the only secondary ice mechanism included in this simulation, rime splintering, is only
220   active at temperatures between $265\,\mathrm{K}$ and $270\,\mathrm{K}$ (Hallett and Mossop, 1974). In a previous study we showed that for the case of (idealized) deep convection secondary ice from rime splintering did not reach the cirrus regime (Lüttmer et al., 2024). In Section 3.4 we will show that the contribution of the SEC ice mode to cirrus in the WCB outflow is also insignificant with less than 0.01%.

As an addition to the above classification scheme we also consider the volume integrated mass and number ratios for each ice
225   mode x

$$g_x = \frac{\int_{t_0}^{t_{end}} \int_{regime} \rho\, q_x\, \mathrm{d}V\, \mathrm{d}t}{\int_{t_0}^{t_{end}} \int_{regime} \rho\, q_{tot}\, \mathrm{d}V\, \mathrm{d}t} \qquad gn_x = \frac{\int_{t_0}^{t_{end}} \int_{regime} \rho\, n_x\, \mathrm{d}V\, \mathrm{d}t}{\int_{t_0}^{t_{end}} \int_{regime} \rho\, n_{tot}\, \mathrm{d}V\, \mathrm{d}t} \tag{3}$$

with the air density ρ. The integration is done along the WCB trajectories from the start time $t_0 = 0\,\mathrm{h}$ to the end time $t_{end} = 48\,\mathrm{h}$. Regime labels one of three cloud types: Mixed-phase clouds containing both IWC and LWC both. Cirrus clouds are defined as pure ice clouds in the cirrus temperature region ($T < T_c = 235\,\mathrm{K}$). And sub cirrus clouds are pure ice clouds below the cirrus temperature region. All WCB trajectory data points outside the respective regime are ignored for the integration. Hence, the integrated mass and number ratios describe how much each ice mode contributes to the overall cloud ice mass content and number concentration in the respective cloud regime.

In addition to the above classification schemes, we also use a Lagrangian classification focusing on the thermodynamic airmass history with the aim of comparing the results from both. This approach closely follows the approach by Wernli et al. (2016): 48 h backward trajectories are started at all grid points with a cirrus cloud. Then the first point along the backward trajectory, at which IWC falls below $q_{crit} = 0.1\,\mathrm{mg\,kg^{-1}}$ is identified, i.e. the time of cirrus formation. If the LWC in this thereby identified cirrus segment is larger than q_{crit} the cirrus cloud is classified as liquid origin, otherwise as in-situ cirrus. Compared to the implementation by Wernli et al. (2016), we (i) employ the approach to the forward trajectory data-set described in Section 2.3 and (ii) explicitly exclude secondary ice from the total cloud ice content considered for identifying cirrus formation. Secondary ice is excluded for consistency with the ice mode classification. Hence, both classification schemes analyse the same cirrus cloud segments, where $q_{tot} - q_{sec} \geq q_{crit}$ and $T < T_c$.

2.5 Observational data used for comparison to simulations

To provide some basic check on the physical realism of the simulations, we compare our ICON model simulations to the CLAAS-2 (CLoud property dAtAset using SEVIRI, Edition 2) observational products, with a focus on Cloud Water Path (CWP) and Cloud Optical Thickness (τ) (Benas et al., 2017). The retrieval algorithm uses SEVIRI visible and near-infrared measurements to obtain the (total) cloud optical thickness τ and the effective radius of cloud particles (r_{ref}) at cloud top. We use the formulae of Stephens (1978) to estimate LWP (Liquid Water Path) as well as IWP (Ice Water Path)

$$\mathrm{LWP} = \frac{2}{3}\rho_w r_{ref}\tau_{opt} \qquad \mathrm{IWP} = \frac{2}{3}\rho_i r_{ref}\tau_{opt} \qquad \mathrm{CWP} = \mathrm{LWP} + \mathrm{IWP} \qquad (4)$$

with the cloud optical thickness τ_{opt}, the effective radius r_{ref} and the liquid water and ice density, ρ_w and ρ_i, respectively. Only a single value of r_{ref} is used to represent all ice crystals in the entire atmospheric column in CLAAS-2. CWP is simply the sum of LWP and IWP. The CLASS-2 CPW data is interpolated onto the model grid for comparison. Only CLASS-2 observations are used that were recorded within $5\,\mathrm{min}$ of a model output time step. Cloud water path for he model simulation is simply computed by vertical integration and summation of all microphysic classes at each grid point.
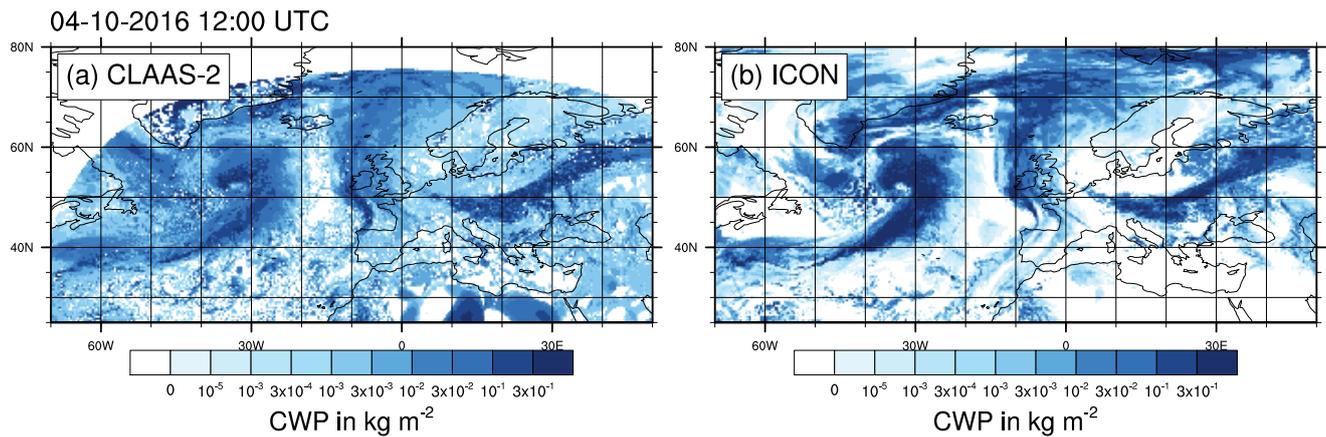
Figure 1. Cloud Water Path (CWP) from CLAAS-2 and the ICON-ice modes simulation for 4th October 2016 12:00 UTC. CLAAS-2 data was regridded to model grid.

3 Spatio-temporal structure of WCB related clouds

3.1 General overview of the cyclone evolution and comparison to observations

The surface cyclone began as a weak surface pressure depression at 2[t]h October 2016 at approximately $45°\,$N and moved over the North Atlantic (Oertel et al., 2023). The cyclone intensified while moving north towards Greenland and showed strong warm and cold sectors with an accompanying WCB from the 4[t]h to 6[t]h October. WCB ascent lead to the development of a vast cloud band with a large cirrus outflow region above Scandinavia. For a detailed discussion regarding the dynamic development of the cyclone and the vertical structure of the associated WCB we refer to the study of Oertel et al. (2023).

The structure of the WCB related cloud in the early mature stages (12 UTC 4[t]h October 2016) of the cyclone is visible in Figure 1, which shows the total Cloud Water Path (CWP) fields from CLAAS-2 retrieval and model data. The WCB associated cloud band forms a characteristic comma-shaped region of high CWP south-east of Greenland. The WCB cloud band is most pronounced at this point in time (Oertel et al., 2023) and gets slightly less sharp and well organised as the cyclone moves towards Europe in the next $48\,$h. The modelled and observed cloud fields show a very similar horizontal extend, geographic position and overall structure, although smaller and scattered clouds are not everywhere consistent between model and observations. However, the modelled clouds contain higher values of CWP, while the CLAAS-2 data shows a larger spatial coverage. Therefore we conclude that the general structure of the WCB related cloud is captured by our ICON simulation, although the vertical water transport and condensate loading seem to be overestimated by the model.
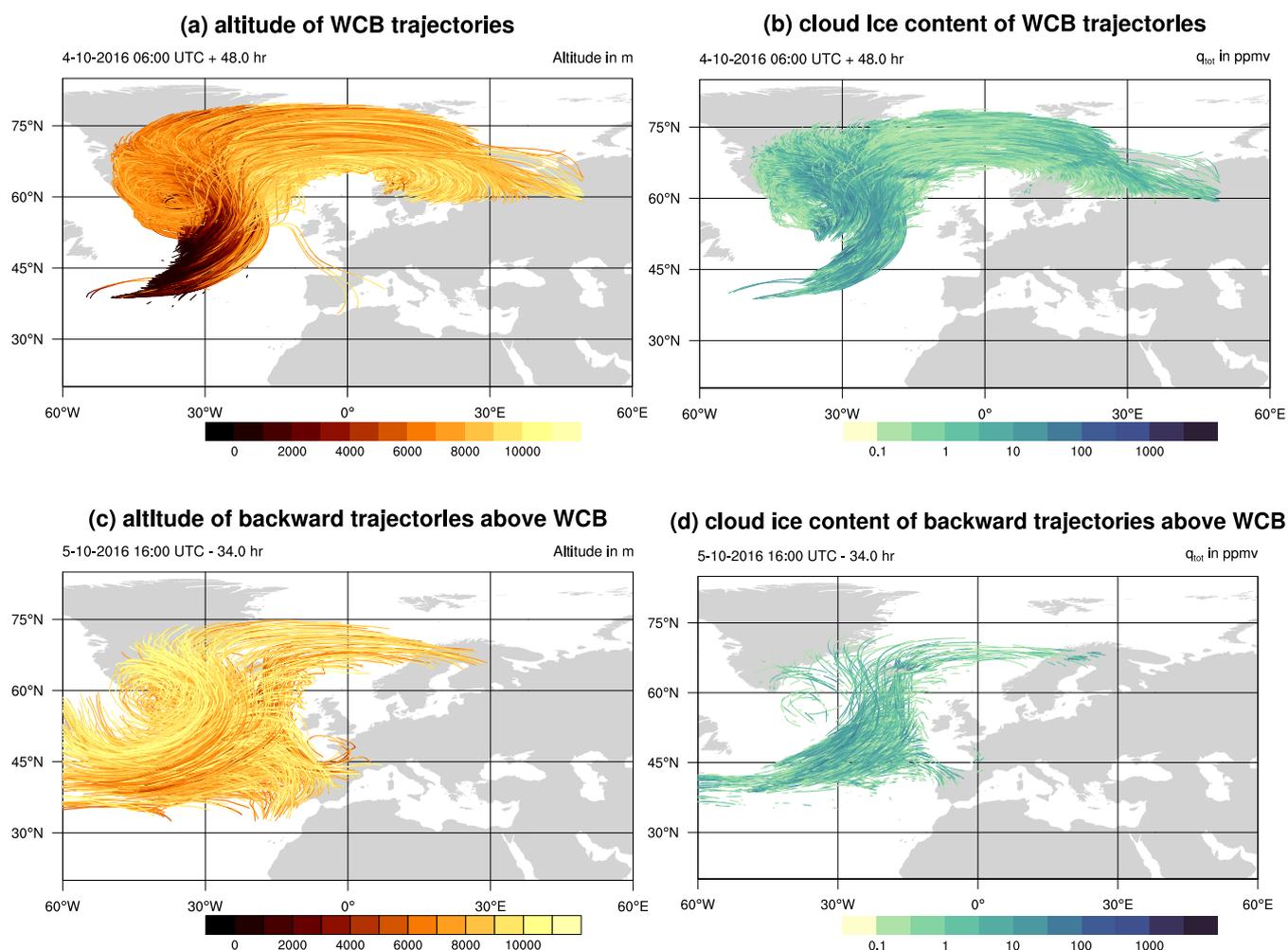
Figure 2. WCB trajectories starting at 4th October 06:00 UTC (a,b) and backwards trajectories started above the WCB at 5th October 16:00 UTC (c,d). Colored according to altitude (a,c) and total cloud ice content (b,d), respectively. Only randomly selected 5 % of all trajectories used in the analysis are shown.

3.2 Structure and distribution of WCB clouds

The general spatial structure of the WCB is shown in Figure 2 (a) and (b), which display the position of WCB trajectories. Overall we identified 40947 WCB trajectories consistent with our criteria for WCB ascent (see Section 2.3), which start predominantly south and east of the surface cyclone center within the warm sector. The WCB air parcel then ascend northward as a dense pack (Figure 2 (a)). When reaching Greenland the WCB trajectories spread: the majority propagates eastwards into an outflow region above Scandinavia, while the other trajectories move westwards towards the cyclone center. High total cloud
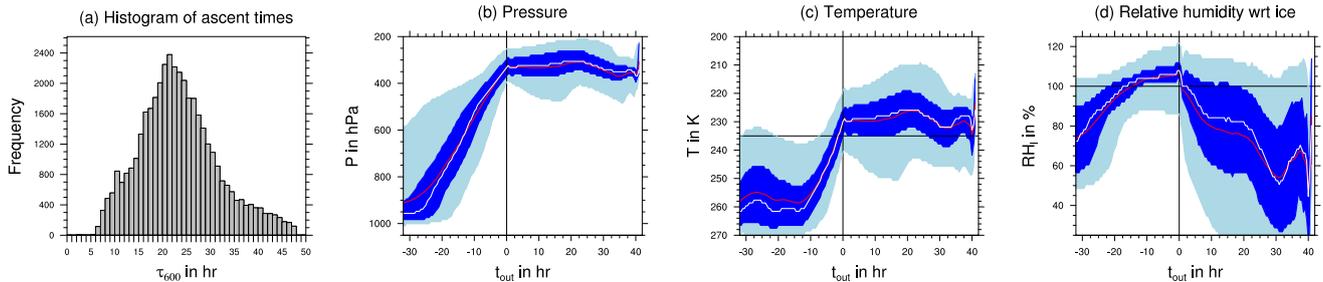
Figure 3. (a) Histogram of WCB (fastest) ascent time τ_{600}. Statistics along WCB trajectories for (b) pressure p, (c) temperature and (d) relative humidity with respect to ice $\mathrm{RH_i}$ are shown as a function of outflow time t_{out}. The median is indicated by a white line, the mean by a red line. The 25th to 75th percentile range is indicated by dark blue shading and the 5th to 95th percentile in light blue shading.

ice content (q_{tot}) up to $5\,\mathrm{ppmv}$ is encountered in the first third of the trajectory paths corresponding to the ascent phase, i.e. region of large altitude changes (Figure 2 (b)).

Figure 2 (c) shows the spatial structure of exemplary backward trajectories above the WCB. As detailed in Section 2.3 this
280 trajectories were started hourly on vertical levels above $7\,\mathrm{km}$ and chosen such that they intersect with WCB trajectories horizontally at least once and stay above $5\,\mathrm{km}$ at all times. Most sample trajectories in Figure 2 (c) stay at altitudes above $8\,\mathrm{km}$ for the entire $34\,\mathrm{h}$ duration. Similar to the WCB trajectories, part of the trajectories propagate eastwards into the outflow region or westwards toward the cyclone center. However, a significant portion of trajectories deviates from the WCB trajectories and move towards Spain. Figure 2 (c) also shows two inflow regions: from the cold sector west of the cyclone center and from the
285 Mid-Atlantic Ocean. Figure 2 (d) shows that the air stream above the WCB has a significant amount of cloud ice. However, it is not as wide spread and area-covering as for the WCB trajectories. The highest values of q_{tot} up to $5\,\mathrm{ppmv}$ are located above the WCB ascent region from $35°$ to $15°\,\mathrm{W}$ (compare Figure 2 (a) and (d)). Ice formed in this air stream can sediment and impact the composition and properties of WCB clouds below. We do not claim that this selection criterion captures all trajectories that might contribute to ice sedimenting into the WCB. However, it will serve as an indication if the sedimentation
290 process is relevant.

The vertical velocity structure of the WCB was identified in earlier studies to be of central importance for diabatic heating and PV modification, moisture transport and precipitation formation pathways (Oertel et al., 2023; Schwenk and Miltenberger, 2024). A commonly used metric to quantify the vertical velocity structure is the WCB ascent timescale τ_{600} defined as the shortest time needed to complete the $600\,\mathrm{hPa}$ WCB ascent along a trajectories. For example, Oertel et al. (2023) showed
295 that the fastest ascending WCB trajectories ($\tau_{600} < 18\,\mathrm{h}$) had experienced stronger heating from liquid phase cloud processes (droplet activation, riming, freezing). In contrast for the slowest ascending WCB trajectories ($\tau_{600} > 30\,\mathrm{h}$) deposition growth of ice phase particles was more pronounced. Therefore τ_{600} may impact ice formation mechanisms and the outflow cirrus derived from particular regions of the ascent, which is explored in later sections. Here we first show the τ_{600} distribution for our WCB trajectory data-set in Figure 3 (a). Note that the histogram excludes trajectories that do not contain a cirrus cloud.
300 Hence, trajectories which never show IWC $< q_{crit}$ and $T < T_c$ at the same time step are excluded. Thus it is not a complete

picture of the dynamical structure of the WCB.

The mean ascent time is $23.27\,\mathrm{h}$. The fastest $5\,\%$ of trajectories need $10.5\,\mathrm{h}$ or less to ascent and represent convective-like ascents. Forming the tail of the distribution are the $5\,\%$ slowest trajectories needing at least $31.5\,\mathrm{h}$ to ascent. These trajectories represent a slow, gradual ascent. These statistics and the general shape of the distribution agree well with distribution derived from high-resolution trajectories for the same case in (Oertel et al., 2023) and in broad agreement with distributions from other cases (Rasp et al., 2016; Oertel et al., 2021, 2023; Schwenk and Miltenberger, 2024). Note, that this study only uses offline calculated trajectories and therefore we are not able to resolve embedded convection. However, Oertel et al. (2023) found that this case only shows a small fraction of embedded convection.

Figure 3 (b) - (d) show statistical distribution of WCB trajectory pressure p, temperature T and relative humidity wrt ice $\mathrm{RH_i}$ as a function of outflow time t_{out}. Outflow time relates to the time step where the trajectory completes is ascent as defined above. Hence the trajectory time is shifted such that the outflow time is 0 when the τ_{600} ascent is completed. Outflow time with negative sign corresponds to the time during and before ascent and with positive sign to the time after ascent. Figure 3 (a) shows the air pressure of the trajectories as a surrogate for altitude. The trajectories rise steadily mostly starting between 975 and $900\,\mathrm{hPa}$ as can be seen from the 25th to 75th percentile in dark blue shading. The statistical distribution at the outflow (for $t_{out} = 0\,\mathrm{h}$) is narrow with most trajectories completing the ascent between 350 and $300\,\mathrm{hPa}$. Most trajectories up to the 95h percentile (shaded in light blue) stay above $375\,\mathrm{hPa}$ for the entire time after ascent.

Figure 3 (c) shows the temperature T distribution experience by the WCB trajectories before and after ascend. Non-fast ascending WCB trajectories ($t_{out} \leq -18\,\mathrm{h}$) show a broad distribution in starting T from 265 to $250\,\mathrm{K}$. However, for the time period before completing ascent ($-10 \leq t_{out} \leq 0\,\mathrm{h}$) T falls rapidly and the statistical distribution is narrow. Almost all ($> 95\,\%$) WCB trajectories complete ascent below the cirrus temperature level $T_c = 235\,\mathrm{K}$ (horizontal black line). The majority of WCB trajectories ($> 75\,\%$) also stay below T_c for the entire time after ascent although the distribution widens as indicated by the percentiles 5/95th and 25/75th percentiles (light and dark blue shading, respectively).

Figure 3 (d) shows the distribution of relative humidity wrt ice $\mathrm{RH_i}$ as a function of t_{out}. Shortly before ascent ($-10 \leq t_{out} \leq 0\,\mathrm{h}$) most trajectories ($> 75\,\%$) are supersaturated wrt ice ($\mathrm{RH_i} > 100\,\%$). After ascent ($t_{out} > 0\,\mathrm{h}$) $\mathrm{RH_i}$ falls rapidly in the sub-saturated regime with a wide statistical distribution due to depletion of supersaturation by depositional growth and mixing with dry air.

In summary, most WCB trajectories experience a similar thermodynamic environment as described by T and $\mathrm{RH_i}$ shortly before ascent ($-10 \leq t_{out} \leq 0\,\mathrm{h}$). T and $\mathrm{RH_i}$ are the most important thermodynamic quantities governing growth by deposition of water vapor and activation of ice formation pathways (see, e.g., Lüttmer et al. (2024)).

3.3 Occurrence of ice modes along exemplary WCB trajectory

Figure 4 shows an exemplary WCB trajectory along which all different ice modes are occurring. This figure illustrates the information available from the ice modes scheme. The standard two-moment scheme would only provide information about the total cloud ice content (TOT) shown in Panel (a). For a detailed comparison between the standard and ice modes scheme we refer to Lüttmer et al. (2024). Panel (b-f) shows the ice modes mass content in a vertical cross section along this sample
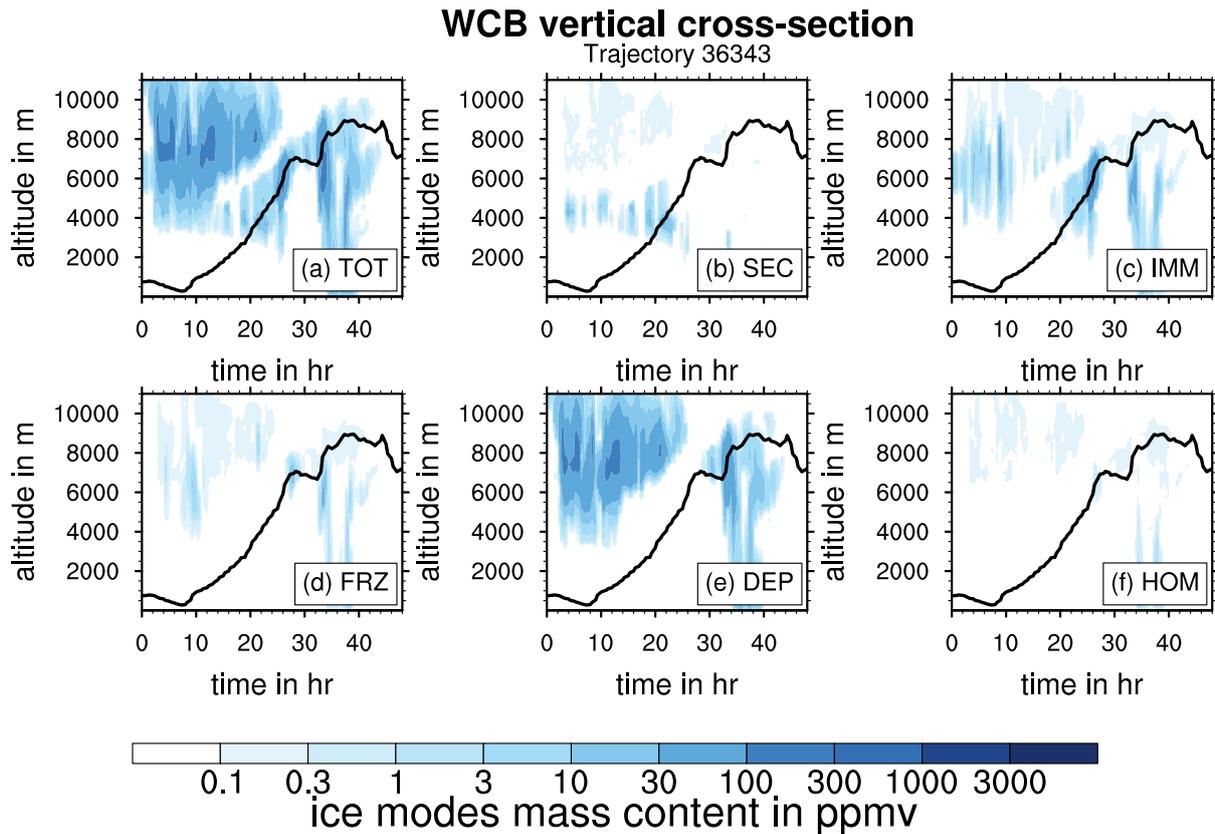
Figure 4. Vertical cross-section of the WCB along a sample trajectory. Profiles are co-located in time and horizontal position with the shown air parcel, the altitude of which is indicated by the black line. Cloud ice mass content for the five ice modes as well as the sum of all ice modes (TOT) is shown by the color coding in the different panels.

335 trajectory. Profiles are co-located in time and horizontal position with the air parcel; the altitude of which is indicated by the black line. The total ice mass is shown in Fig. 4 a: The considered air parcel starts its ascent close to the surface below $1\,\mathrm{km}$ altitude and ice first occurs in the air parcel after $20\,\mathrm{h}$ at an altitude of about $3\,\mathrm{km}$. This first ice belongs mainly to the SEC ice mode consistent with strong SEC formation region in the Hallett-Mossop temperature range just below $0\,°\mathrm{C}$ (Fig. 4 b). Here, also graupel is formed which sediments from the deep WCB clouds extending to higher altitudes. As the parcel moves to

340 higher altitudes and lower temperatures, frozen droplets primarily stemming from IMM form the ice phase in the cloud layer above ($\approx 25\,\mathrm{h}$, Fig. 4 c). Following the parcel even further upward, the parcel reaches a ice layer consisting predominantly of homogeneously frozen cloud droplets (FRZ, $\approx 28\,\mathrm{h}$, Fig. 4 d). Finally at the lowest temperatures in the trajectory ice crystals formed by deposition nucleation (DEP) are found ($\approx 32\,\mathrm{h}$, Fig. 4 e). Between 30-40 h, we observe fall streaks of sedimentating ice stemming of the DEP mode. Sedimentation connects upper level ice formation region to lower altitudes.
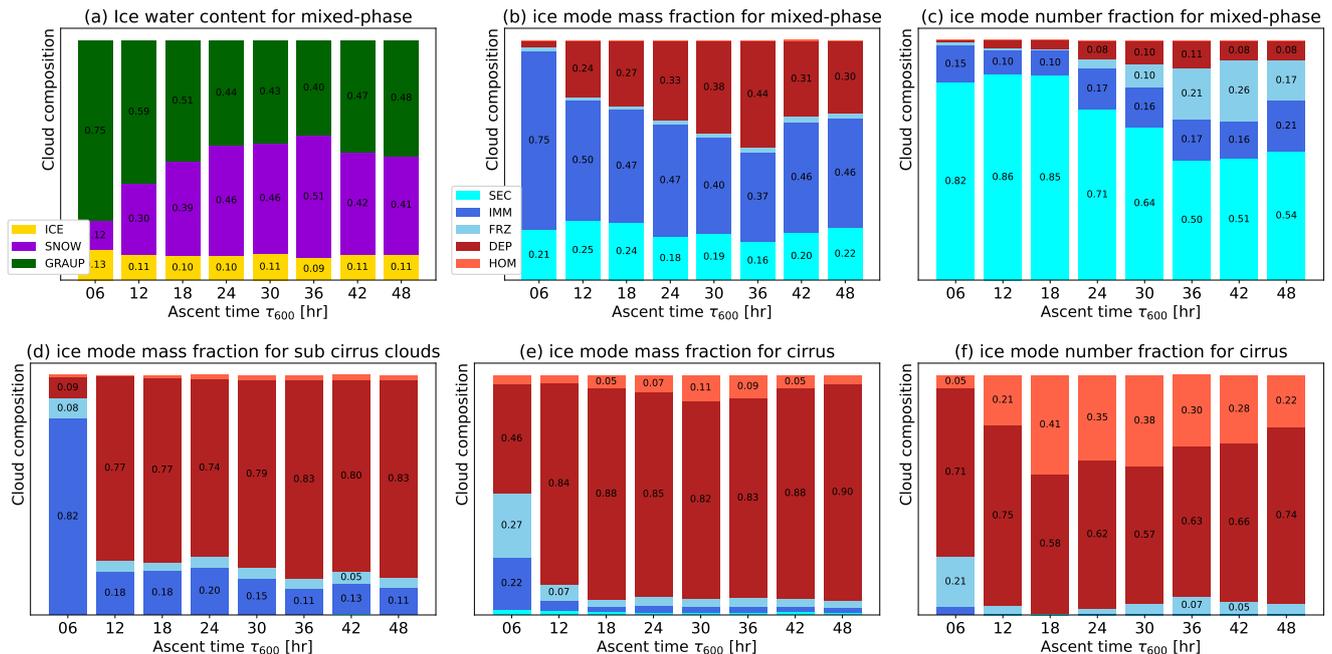
Figure 5. Relative contribution of the different frozen hydrometeor types (a) and different ice modes (b-f) to the ice mass (a, b, d, e) and ice number (c, f) as function of the ascent timescale τ_{600}. Panels (a-c) show results for mixed-phase clouds, panel (d) for the pure ice-cloud at sub-cirrus temperatures, and panel (e, f) for cirrus clouds. We only display value labels for relative contributions ≥ 0.05. The x-axis labels signify the upper limit of the respective ascent timescale bin.

345 The vertical sequence of layers dominated by specific ice modes is overall similar to that found for the deep convection case in Lüttmer et al. (2024) and broadly consistent with the temperature regimes, in which the different ice formation mechanisms are active albeit with (regionally) large modifications by sedimentation.

3.4 Statistics of ice modes distribution for WCB clouds

In the previous section we have shown the vertical structure of mixed- and ice-phase WCB clouds along a single trajectory.
350 We now evaluate this across all trajectories in our WCB data-set, which is stratified according to the WCB ascent time τ_{600}. We further sub-divide the data into mixed-phase cloud (liquid and ice hydrometeors present), sub cirrus cloud (only ice hydrometeors present and $T > 235\,K$), and cirrus clouds ($T \leq 235\,K$). These three categories cover all thermodynamic regimes in which ice can exist in clouds. Figure 5 shows the bulk mass and number partitioning for different cloud types and ascent times. The partitioning is quantified as the ratio of the mass content (or number concentration) of an ice mode (or microphysics
355 class) to the integrated mass content (or number concentration) for all trajectories within that ascent time bin for the specified cloud regime (see Section 2.4 for details).

Mixed-phase clouds

First, we discuss the microphysical composition of the mixed-phase WCB clouds (Figure 5 a-c). Although this is not the focus
of our study, it is still important to quantify as the liquid origin pathway is determined by the transport of liquid or already
frozen droplets into the cirrus temperature regime. About 90 % of the frozen particle mass in the mixed-phase clouds is found
in graupel and snow hydrometeor class (Figure 5 a). Fast ascending trajectories ($\leq 18\,\mathrm{h}$) have larger contributions by graupel
than more slowly ascending parcels consistent with larger riming rates for these trajectories found by Oertel et al. (2023). The
smaller contribution of snow for fast ascent time is likely due to less time for aggregation to occur as well as enhanced loss of
snow and ice particles by collisions with supercooled liquid to form graupel.

In terms of the contribution of different ice formation mechanisms, frozen droplets (IMM and FRZ) provide the largest contri-
bution to cloud ice mass in the mixed-phase cloud regime ($\approx$ 40-75 % depending on τ_{600}, Figure 5 b). However, FRZ takes up
only a small portion of the mass budget. The IMM and FRZ mode compete for available cloud droplets. However, immersion
freezing (IMM) is more efficient and triggers at higher temperatures than homogeneous freezing (FRZ). In this case study there
are enough INP available to freeze cloud droplets by immersion freezing before they are transported to low enough tempera-
tures for homogeneous freezing of cloud droplets. There is a small trend towards increasing contribution of IMM for shorter
ascent timescales. Although this trend is strongest for the fastest ascending trajectories (τ_{600} <6 h), which only constitute
0.001 % of all trajectories. This trend correlates with the decreasing snow contributions and is consistent with the hypothesis
that aggregation is a major sink for IMM mode ice (see also Lüttmer et al. (2024)).

The second largest contribution in terms of ice mass stems from the DEP mode. As deposition nucleation does not occur in
mixed-phase clouds this is a surprising finding and suggests substantial sedimentation from higher-altitude clouds into the
WCB mixed-phase clouds. This is consistent with the fall streaks of DEP ice mode mass seen along the exemplary trajectory
in Fig. 4. Note that the contribution of DEP to the total ice number concentration is comparatively small (Figure 4 c). This
indicates that DEP ice particles are generally large resulting in high fall-speeds and sedimentation rates.

The next largest contribution is secondary ice (SEC) accounting for about 20 % of the ice mass for all ascent times. For the ice
number concentration SEC is the dominant contribution at mixed-phase temperatures (Figure 5 c). The only source term for
SEC in this study is a representation of rime splintering ('Hallet-Mossop process'). The strong SEC contribution is consistent
with the large graupel contribution and therefore likely large riming rates (Figure 5 a). Recent studies suggest that physical un-
derstanding of rime splintering is severely lacking (Korolev et al., 2020) and that rime splintering cannot be observed in recent
laboratory set-up (Seidel et al., 2024). Thus, the model representation of SEC is highly uncertain and may be overestimated
or have an unrealistic temperature structure. However, this does likely not impact our main results strongly, as the SEC mode
does not reach the cirrus temperature regime.

Finally, the HOM mode is not present within the mixed-phase clouds as homogeneous nucleation only occurs at high supersatu-
rations wrt ice ($S_i > 1.35$) and low temperatures. That is outside the thermodynamic regimes of mixed-phase clouds. Although
it is still possible for HOM to sediment into a mixed-phase clouds, the homogeneous nucleation events above the WCB are
mostly suppressed by DEP nucleation as we will discuss later.

Ice-phase clouds at $\geq 235\,\text{K}$ ("sub cirrus clouds")

Mainly in the upper part of the WCB ascent region, pure ice clouds with temperatures above $235\,\text{K}$ occur. Hence, thermody-
namically supercooled liquid would be supported, but clouds are already fully glaciated and these clouds can be viewed as
transition regime between mixed-phase and cirrus clouds. We refer to these clouds as "sub cirrus clouds" in the following.
Figure 5 d shows the contribution of different ice modes to the entire ice mass in the sub cirrus WCB clouds. The DEP mode
provides the largest ice mass contribution with about $80\,\%$ followed by IMM and then FRZ. In addition, there is a small contri-
bution by homogeneous nucleation. Only for the few trajectories with $\tau_{600} \leq 6\,\text{h}$ the IMM ice modes dominates the ice mass.
Compared to the mixed-phase regime, (likely) sedimentation of DEP and HOM ice crystals becomes even ore important as
well as FRZ and the impact of IMM reduces strongly.

Ice-phase clouds at $< 235\,\text{K}$ (cirrus clouds)

Finally, we discuss the contribution of different ice modes to the ice mass and number concentration of WCB derived cirrus,
i.e. pure ice-phase clouds at temperatures lower than $235\,\text{K}$. Figure 5 e and f show the contributions of the different ice modes
to the ice mass and number concentration, respectively. Ice formed through in-situ pathways (DEP + HOM) dominates both the
total ice mass and number concentration. DEP and HOM are in this temperature regime in direct competition for available su-
persaturation. Since homogeneous nucleation requires lower temperatures and higher supersaturation over ice than deposition
nucleation. The latter typically occurs first along in ascending WCB air parcel, provided INP are available. Deposition on DEP
ice can then suppress further (homogeneous) nucleation events by depleting the supersaturation. In this case DEP dominates
over HOM, especially with regard to the cloud ice mass budget. Notably, parcels with intermediate ascent times (18 to $30\,\text{h}$)
show a higher contribution of HOM ice than the faster or slower ascending parcels.

For the fastest ascending trajectories, there is still a substantial contribution of ice of liquid origin (IMM + FRZ), which makes
up about 50 % of the ice crystal mass. However, note again that this category is populated only by very few trajectories.

Overall the DEP ice mode provides a substantial contribution to the ice mass and number density in all cloud regimes and
ascent times. In-situ ice is thus the main constituent of the cirrus in the WCB outflow. Fast ascending trajectories show more
efficient mixed-phase cloud processes (e.g. riming) and higher ratios of liquid origin ice in the resulting cirrus clouds. We will
investigate the contributions of liquid origin and in-situ origin to the WCB cirrus in more detail in Section 4.1.

3.5 Structure and evolution of ice-clouds forming above the WCB ascent region

The flow passing above the WCB often contains additional cirrus clouds that form in airmasses lifted due to the strong vertical
motion below but not ascending sufficiently to pass the WCB criterion. The results in Section 3.4 indicate sedimentation of ice
crystals formed in these above-WCB clouds substantially influences WCB clouds through sedimentation. We therefore also
consider in detail the spatio-temporal location and microphysical structure of the above-WCB clouds.

Figure 2 (c) - (d) illustrates the air flow above the WCB for one exemplary start date. The trajectory data-set used to characterize
the above-WCB flow is described in Section 2.3. The key ice containing air stream starts over the Northern Atlantic and follows
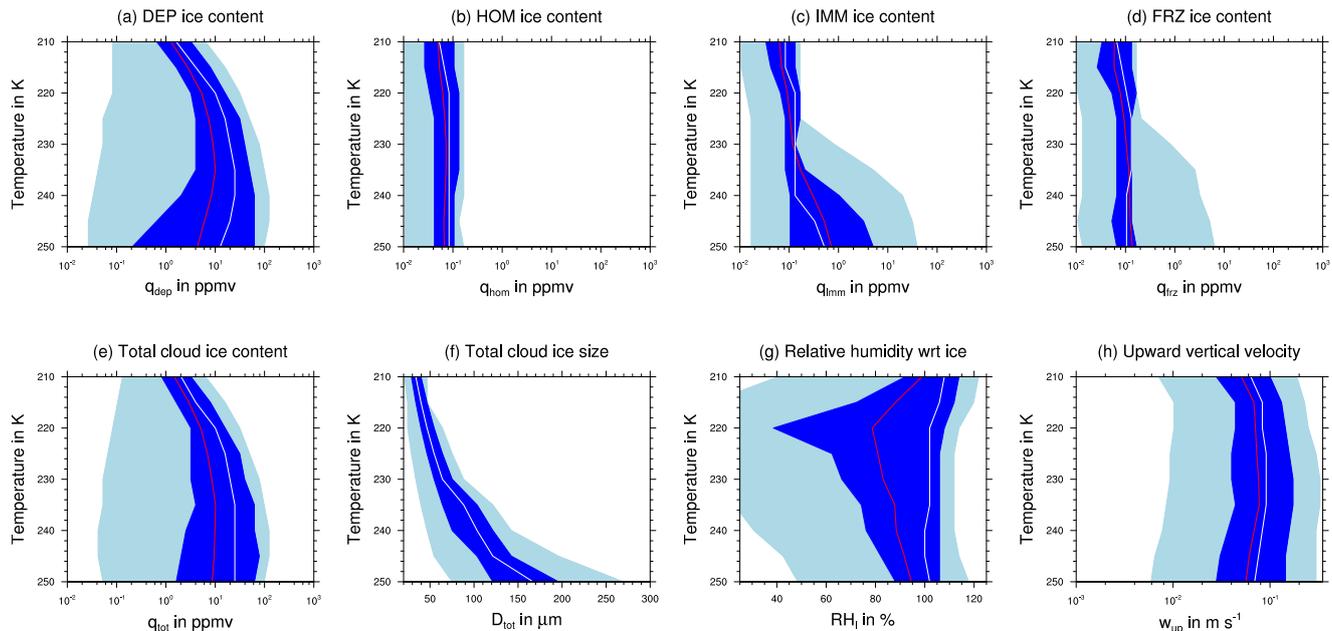
Figure 6. Statistics of the mass content of the different ice modes q_{dep}, q_{hom}, q_{imm}, q_{frz}, the total cloud ice mass content q_{tot}, mean cloud ice size D_{tot}, relative humidity wrt ice RH_i and upward vertical velocity w_{up} as a function of temperature. The median (mean) of each variable is shown by the white (red) line, the 25th to 75th percentile range by dark blue shading and the 5th to 95th percentile in light blue shading.

the movement of the surface cyclone northeastwards. A portion of the parcels follow in the WCB outflow region while some take a more southerly path towards Spain. Many of the trajectories show high IWC especially while located above the WCB. This is another indication that a substantial amount of ice is formed above the WCB. This ice can sediment into lower lying
430   WCB clouds and may be important for the microphysical composition of WCB clouds.

Figure 6 summarizes the microphysical and thermodynamic properties of the air stream above the WCB. For the statistics we only consider data points that are above a WCB trajectory at a given time step and where a ice phase cloud is present ($q_{tot} \geq q_{crit}$). The statistics are shown as a function of air temperature, as this is a crucial parameter for ice microphysical processes. Above-WCB air parcels are found at temperatures between 250 and 215 K. This is related to the selection criterion
435   that the trajectories have to stay above 5 km (see Section 2.3). The total ice water content generally decreases with altitude as does the average size of ice particles (Figure 6 (e) and (f)). The major of ice mass is allocated on particles formed by deposition nucleation (DEP mode, Figure 6 (a) - (d)). The fall streaks of ice from DEP shown in Figure 4 and high contribution of DEP to the mixed-phase WCB clouds shown in Figure 5 likely stem form ice formed above the WCB.

At temperature above 235 K, the IMM mode contributes substantially to the total ice mass. This suggest the presence of ice
440   formed in mixed-phase clouds, likely due to air parcels ascending from the mid-troposphere but not fulfilling the 600 hPa

ascent threshold used for identifying WCB ascent.

Key determinants for the activity of deposition and homogeneous nucleation are the vertical velocity and the supersaturation over ice. The median of vertical velocity lies mostly between 6 and $8\,\mathrm{cm\,s^{-1}}$ with the 75th percentile being larger than $10\,\mathrm{cm\,s^{-1}}$ (Figure 6 h). The median relative humidity over ice RH_i is between 100 and $110\,\%$ (Figure 6 g). According to Krämer et al. (2020) the slow updraft velocities would imply a cirrus with few but large ice crystals from heterogeneous nucleation. However, the relatively low RH_i are below the critical supersaturation needed for homogeneous nucleation (see Lüttmer et al. (2024)). The RH_i are consistent with an existing cirrus cloud (Krämer et al., 2020), but may not be representative of the cirrus formation conditions. However, at the described thermodynamic conditions the deposition nucleation parameterisation (Hande et al., 2015) is active, suggest together with the strong contribution from the DEP ice mode to the total hydrometeor mass, that deposition nucleation is the key ice formation mechanism for above WCB ice clouds.

Mean cloud ice diameter (D_{tot}) increases with increasing temperature and hence decreasing altitude. Hence larger ice crystals (mean size > 100 μm) sediment from the regime suitable for deposition nucleation into the WCB below. Overall this statistics show that DEP ice is present above the WCB showing high mean mass content and strong signatures associated with sedimentation.
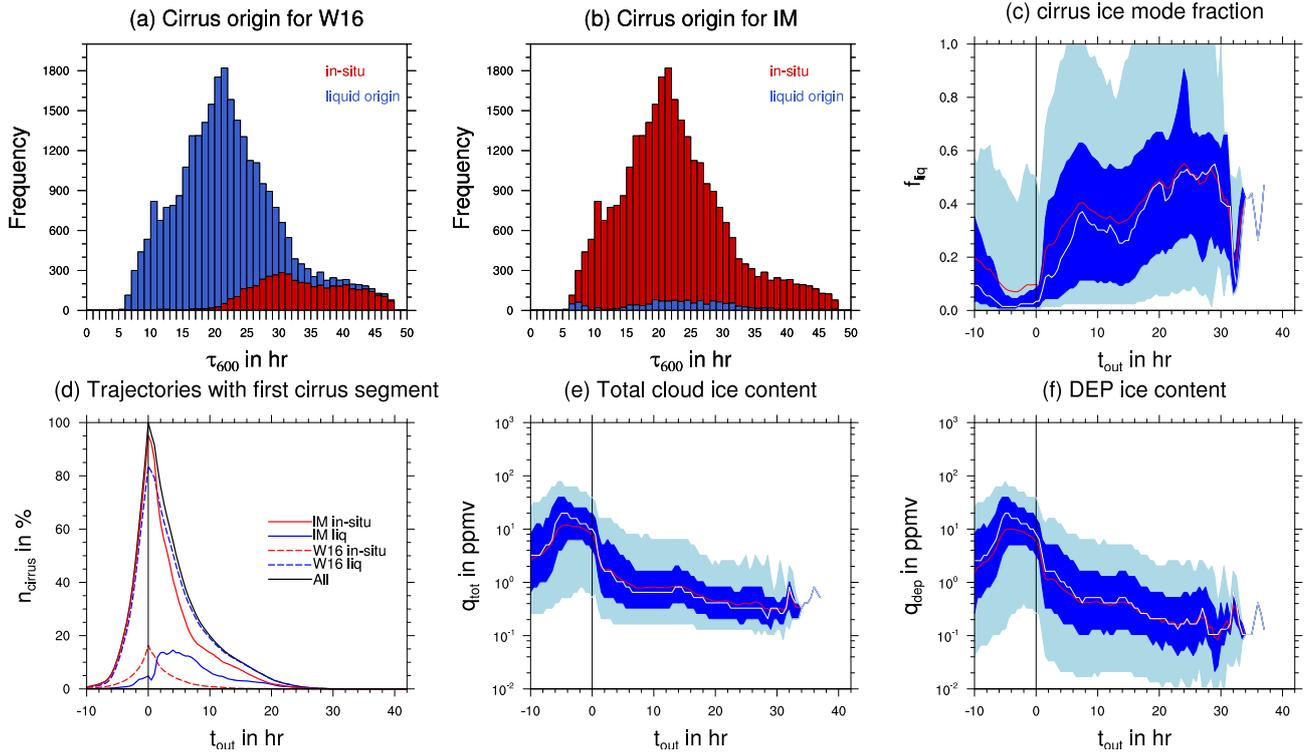
Figure 7. Histogram of WCB ascent timescale τ_{600} colored by cirrus cloud origin according to (a) W16 and (b) our ice modes based classification, respectively. Panel (c) shows the liquid origin fraction as a function of time after ascent t_{out} with the mean (median) indicated by a red (white) line and the 25th to 75th (5th to 95th) percentile range by dark (light) blue shading. Panel (d) shows the percentage of trajectories containing a (first) cirrus segment in the outflow for all segments (black), ice modes in-situ (red), ice modes liquid origin (blue), W16 in-situ (red dashed), W16 liquid origin (blue dashed). Panels (e) and (f) show the total ice water content and the ice water content of DEP, respectively.

4 Characteristics of in-situ and liquid origin cirrus

The question of cirrus origin can be posed by either asking about the thermodynamic history of cirrus parcels or asking about the initial formation of the ice crystals found in a particular cirrus parcel. In the previous section, we have shown that the later maybe substantially modified by sedimentation of ice crystals from low temperatures into mixed-phase ascending WCB parcels. As the main motivation for a classification of cirrus clouds is to explain the wide variance of cirrus properties, we here investigate the (modelled) cirrus properties and their difference between in-situ and liquid origin parcels, where the classification is ones based on thermodynamic history (following W16) and ones based on our ice modes scheme (IM).

Classification	Ascent		All	
	liquid origin	in-situ	liquid origin	in-situ
Ice modes	10 %	90 %	16 %	84 %
W16	84 %	16 %	64 %	36 %

Table 1. Cirrus cloud composition following the ice modes and W16 classification. Ascent only includes the first type of cirrus encountered after WCB ascent (τ_{600}). All includes all points of the WCB trajectory where cirrus is present.

4.1 Comparison of cirrus classification

First we compare the results from applying the W16 algorithm (modified for use with forward-trajectories as described in Section 2.4) and the ice modes-base classification. Figure 7 (a) and (b) show histograms of WCB (fastest) ascent times τ_{600} colorcoded with the result of the classification (not that the histogram without colorcode is the same as shown in Figure 3 (a)). Trajectories are colored according to the first type of cirrus cloud encountered by the trajectory after fulfilling the $600\,\mathrm{hPa}$ ascent criterion. If a cirrus clouds is found at the end of the τ_{600} segment, the color corresponds to the classification of the cloud segment wherein τ_{600} is fulfilled for W16 and to the liquid origin fraction f_{liq} at the time step where τ_{600} is fulfilled for the ice modes based classification. If there is no cirrus cloud present at end of ascent, but later on a cloud forms ($q_{tot} \geq q_{crit} = 0.1\,\mathrm{mg\,kg^{-1}}$), the cloud type is projected back to the original ascent time. Note, that in the ice modes based classification, a cloud with $f_{liq} > 0.5$ is considered a liquid origin cirrus cloud and otherwise an in-situ cirrus cloud.

Figure 7 (a) shows that W16 identifies the majority (84 %) of WCB cloud segments at the end of the τ_{600} segment as liquid origin cirrus. In-situ cirrus is mostly identified at high ascent times ($> 25\,\mathrm{h}$) and in the tail-end of the distribution. That shows that many cloud segments persist as clouds from the mixed-phase into the cirrus cloud regime (without q_{tot} dropping below q_{crit}), as only then are they classified as liquid origin by W16 (see Section 2.4).

Figure 7 (b) shows the cirrus origin after ascent as determined by the microphysical composition determined with the ice modes scheme. The fraction of liquid origin cirrus is very low (10 %) in stark contrast to the 84 % found with the W16 algorithm. The liquid origin cirrus are found in substantial relative frequency only for the fast ascent regime ($< 18\,\mathrm{h}$). In addition some also appear in the intermediate ascent regime. This is consistent with our earlier findings in Section 3.4 that fast ascending trajectories show enhanced activity of mixed-phase processes (esp. riming) and higher mass fractions of frozen droplets (IMM

and FRZ). The results from applying the W16 algorithm suggests that many cloud segments show a continuous cloud from the mixed-phase deep into the cirrus regime, which would imply a dominance of liquid-origin cirrus at end of ascent. However, sedimentation of DEP ice from clouds above the WCB is abundant (see Section 3.5). This makes DEP the predominant ice mode leading to an in-situ cirrus classification for the majority of parcels.

So far we have only considered the liquid origin and in-situ classification of the cloud segment directly after fulfilling the (fastest) ascent criterion τ_{600}. Table 1 shows the classification including all cloud segments where cirrus clouds are present in the WCB trajectories, i.e. also including cloud segments that are separate by segments of clear sky conditions from the cloud formed during WCB ascent. The ice modes classification only differs slightly with an 6% increase of in-situ cirrus abundance and a corresponding decrease for liquid origin cirrus. Hence ice from DEP and HOM mode dominate the cirrus composition during (almost) all times. Classification following W16 suggests an increase of 20% in in-situ cirrus abundance, as cirrus clouds forming disjunct from the WCB ascent cloud band are likely formed at low temperature and below water saturation. Still there remains a large 'disagreement' with the ice modes scheme.

In summary, the classifications of cirrus according to thermodynamic pathway (based on W16 algorithm) and according to initial ice formation processes do not agree. To interpret the differences and to understand their importance for cirrus properties, we have to consider the different definition of in-situ and liquid origin in both approaches. In this study the liquid origin fraction is determined entirely by the formation mechanism of the ice particles. Whether that is the sole determinant of the cirrus properties or whether growth conditions and microphysical processes encounter along the trajectories are more important for the outflow cirrus properties needs to be determined. For example, if a parcel passed trough a mixed-phased clouds it was thus subject to riming, aggregation and strong depositional growth (Wernli et al., 2016), which might lead to higher ice water content and larger ice particles than for cirrus clouds that only experience the thermodynamic environment of the upper troposphere. In that case the W16 trajectory based algorithm is useful in determining which cirrus clouds recently experienced mixed-phase cloud processes. By applying both classifications and then comparing the microphysical properties as well as their evolution for our case, we address this question in the Section 4.3 after considering the temporal evolution of microphysical properties along all outflow trajectories (Section 4.2.

4.2 Evolution of cirrus properties in WCB outflow (incl. liquid fraction)

We will now investigate the cirrus properties before and after end of ascent ($t_{out} = 0$ h). For the analysis we only consider the first cirrus segment that exists at end of ascent. Parcels with cirrus segments ($q_{tot} > q_{crit}$ and $T < T_c$) are included in the statistics for the time period in which they contain a cirrus cloud. We apply this additional selection criterion as we cannot clearly associate the (possible) formation of subsequent cirrus segments with the ascent of the WCB.

Figure 7 (d) shows the percentage of WCB trajectories with cirrus segments n_{cirrus} contributing to the statistics shown in the following as a function of outflow time t_{out}. Here we are only interested in the black line that includes all cirrus segments independent of classification. We will discuss the percentage of cirrus fragments belonging to the respective classifications in Section 4.3. As we only consider WCB trajectories with a cirrus segment at $t_{out} = 0$ h, n_{cirrus} equals 100% for $t_{out} = 0$ h by construction. At $t_{out} = 10$ h n_{cirrus} falls to 20% as most initial cirrus cloud segments have dissolved through sublimation

or sedimentation. At $t_{out} = 24\,\mathrm{h}$ n_{cirrus} is below 1%, thus the statistics after this time contains only a few rare parcels with persistent cirrus clouds.

In Section 2.4 we introduced the liquid origin (mass) fraction f_{liq}, which quantifies the degree to which a (cirrus) cloud is made from ice formed by in-situ or liquid origin formation processes. A liquid origin fraction close to 1 classifies the cirrus as liquid-origin and close to 0 as in-situ. Figure 7 (c) shows the statistical distribution of the cirrus liquid origin fraction of clouds as a function t_{out}. Before ascent (black line) most of the trajectories are dominated by in-situ formed ice (median and 75th percentile below $f_{liq} = 0.15$). The liquid origin fraction rapidly drops further at ascent ($t_{out} = 0\,\mathrm{h}$), where the distribution is very narrow. Liquid origin ice has likely sedimented out of the trajectory at this point and in-situ ice formation processes within or above the WCB dominate the microphysical composition of the cirrus cloud. This also agrees with the results shown in Figure 7 (b) which also show the dominance of in-situ formed ice at $t_{out} = 0\,\mathrm{h}$.

Almost none of the WCB trajectories reach liquid origin fractions close to 1 after ascent. However, the liquid origin in general increases up to a mean (red line) of 0.5 for the few parcels, in which the cirrus segment persists longer than $20\,\mathrm{h}$. This is likely a result of ice with large masses formed by in-situ processes sedimenting out of the WCB trajectories, but remnants of ice formed by liquid origin process with very small masses remaining. Thus, a few hours after ascent the WCB trajectories contain only thin cirrus. This cirrus is a remnant of ice from different formation pathways. The thin nature of the outflow cirrus is also evident when considering the total ice mass content q_{tot} shown in Figure 7 (e): q_{tot} reduces by more than one order of magnitude in the first $10\,\mathrm{h}$ after end of ascent. The DEP ice mass content, the dominant in-situ icemode in the considered clouds, shown in Figure 7 (f) behaves very similar to q_{tot}, i.e. decreasing rapidly after $t_{out} = 0\,\mathrm{h}$.

4.3 Evolution of microphysical properties along in-situ and liquid origin cirrus parcels

We now compare the evolution of microphysical properties in the sub-sets of cirrus parcels classified as either in-situ or liquid origin by the W16 and our ice modes-based classification IM. We contrast the in-situ to liquid origin difference of cirrus properties in both classification schemes and compare to typical cirrus characteristics of strongly ascending WCB trajectories as found in existing literature [see, Luebke et al. (2016); Wolf et al. (2018); Krämer et al. (2020)]. Not that the IM classification is a point-wise classification. Hence it can change each time step opposed to the W16 classification which classifies an entire cirrus segment (see Section 2.4). Figure 8 shows the time evolution of total ice content (top row), total ice number concentration (middle row), and liquid origin fraction (bottom row). The evolution is shown separately for cirrus classified as (i) liquid origin by W16 (a,e,i), (ii) liquid origin by the ice modes based classification (IM) (c,g,k), (iii) in-situ by W16 (a,e,i), and (iv) in-situ by the ice modes based classification (d,h,l).

W16 liquid origin

In cirrus segments classified as liquid origin by W16 (84% of all WCB cirrus parcels; **"W16 liquid origin"** in the following) the total ice content q_{tot} peaks $-5\,\mathrm{h}$ before ascent is completed (Figure 8 a). At its peak the median q_{tot} is $20\,\mathrm{ppmv}$, which is within the range given for ice content of liquid origin cirrus in literature (Krämer et al., 2020). The ice content rapidly falls below $10\,\mathrm{ppmv}$ after the end of ascent and continues to decrease until the end of the considered time period. However, the
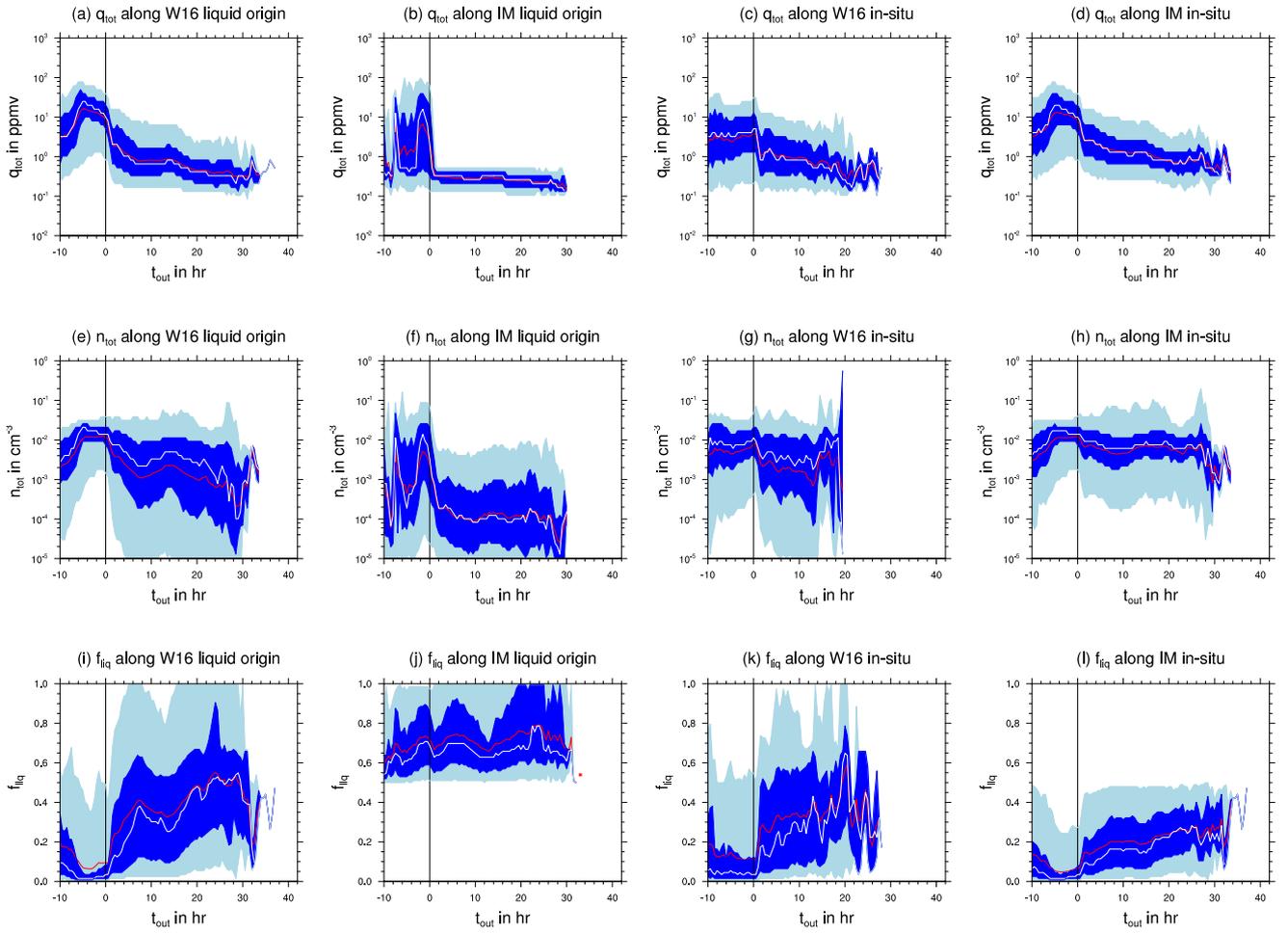
Figure 8. Statistics of total ice content q_{tot} (a-d), total ice number density n_{tot} (e-h) and liquid origin fraction f_{liq} (i-l) along liquid origin and in-situ sections as identified by W16 (first and third column) and ice modes based method (second and fourth column) for the first cirrus segment after end of ascent. The median (mean) of each variable is represented by the white (red) line, and the 25th to 75th (5th to 95th) percentile range by dark (light) blue shading.

width of the distribution (quantified by the interquartile range) changes only slightly and remains at about one order of magnitude. Figure 8 (e) shows the evolution of total ice number concentration n_tot. n_{tot} reaches its maximal value of $0.01\,\mathrm{cm^{-3}}$ during the ascent phase, which is below values for (idealized) liquid origin cirrus ($0.05-2\,\mathrm{cm^{-3}}$) stated in previous literature (Krämer et al., 2020). As q_{tot}, n_{tot} is also decreasing after ascent but not as strongly. Finally, we consider the information on ice formation pathways from the ice modes schemes for the subset of cirrus that are classified as liquid-origin by W16. Figure 8 (i) shows the liquid origin fraction f_{liq}. f_{liq} is very low (close to 0) between -6 and $0\,\mathrm{h}$. At $-6\,\mathrm{h}$ parcels are located in the mean at about $500\,\mathrm{hPa}$, i.e. about 100-200 hPa below outflow level, temperatures of about $-30\,^{\circ}\mathrm{C}$, and parcels are typically fully glaciated (Figure 3). During this time period the total ice content q_{tot} reaches its maximum along the trajectories (Figure 8 (a)). At these conditions one would expect a much stronger influence of ice formation processes operating at water saturation, but sedimentation of ice from higher altitudes and temperatures below the homogeneous freezing temperature (235K) dominates ice number concentration and thereby ice mass in this region of the WCB air stream (see also discussion in Section 4.1). Very efficient removal of ice formed at warmer temperatures through mixed-phase processes may further contribute to this signal (Schwenk and Miltenberger, 2024).

IM liquid origin

In cirrus segments classified as liquid origin by our IM based method (10% of all WCB cirrus parcels, **"ice mode liquid origin"** in the following) total ice content q_tot also reaches its maximum before end of ascent ($t_{out} = -2\,\mathrm{h}$) (Figure 8 (b)). Despite a similar absolute value, q_{tot} overall has a large variability during the ascent phase compared W16 liquid origin cirrus. This may be a consequence of the small number of IM liquid origin parcels or reflect a large diversity in microphysical properties. After end of ascent, mean q_{tot} falls very rapidly below $1\,\mathrm{ppmv}$ and remains almost two orders of magnitude below the maximum q_{tot} value until the end of the considered time period. This is consistent with liquid origin cirrus classified by our IM classification to be optically very thin, as discussed in Section 4.2. Compared to W16 liquid origin parcels q_{tot} is about a factor 2 smaller in the first $24\,\mathrm{h}$ of the outflow cirrus lifetime. The total ice crystal number concentration n_{tot} behaves similar to q_tot with a peak in the ascent phase and rapid decrease afterwards (Figure 8 (f)). In the outflow ($t_{out} > 0\,\mathrm{h}$) n_tot varies over about two orders of magnitude across parcels (interquartile range) with a mean n_tot of about $10^{-4}\,\mathrm{cm^{-3}}$. Hence, the mean n_{tot} is about one order of magnitude lower than in W16 liquid origin cirrus. By construction all f_{liq} values are above 0.5 for IM liquid origin cirrus parcels (Figure 8 (j)). The median value is consistently around 0.75 indicating that at least 50% of cirrus parcels are substantially influenced by ice formed by in-situ formation processes.

W16 in-situ origin

In cirrus segments classified as in-situ origin by W16 (16% of all WCB cirrus parcels, **"W16 in-situ"** in the following), q_{tot} in the ascent phase remains almost constant and with a mean value around $3\,\mathrm{ppmv}$ almost one order of magnitude smaller than the maximum value reached in W16 liquid origin (Figure 8 (c)). After the ascent q_{tot} decreases continuously reaching similar values to W16 liquid origin cirrus. The median of n_{tot} remains about a factor 2 lower in the ascent compared to W16 liquid origin (Figure 8 (g)). In the outflow phase the mean n_{tot} is around $0.01\,\mathrm{cm^{-3}}$, which is similar to W16 liquid origin but much

larger than in IM liquid origin cirrus. n_{tot} is in the range expected for slow updraft in-situ cirrus (Krämer et al., 2020). The liquid origin fraction f_{liq} behaves qualitatively similar to W16 liquid origin parcels (Fig. 8 k). Hence, differences between W16 liquid origin and in-situ cirrus are mainly found in the ascent phase ($t_out <0\,\mathrm{h}$), while in the outflow phase cirrus in both categories show very similar properties.

IM in-situ origin

Finally, we consider cirrus segments classified as in-situ origin by our IM method ($84\,\%$ of all WCB cirrus parcels at ascent, **"ice modes in-situ"** in the following). q_{tot} reaches its largest values of about $10\,\mathrm{ppmv}$ at $t_{out} =-6\,\mathrm{h}$ and only slightly decreases until $t_out =0\,\mathrm{h}$ (Figure 8 (d)). These values are more consistent with those previously reported for liquid origin cirrus (Krämer et al., 2020). After end of ascent q_{tot} decreases continuously, but remains about a factor 2 above values for both W16 cirrus categories and about a factor 3 above values found for IM liquid origin cirrus. The evolution of n_{tot} in the ascent phase strongly resembles that of W16 liquid origin cirrus with a maximum value of $0.02\,\mathrm{cm}^{-3}$ reached at about $t_{out} =-6\,\mathrm{h}$ (Figure 8 (h)). At $t_{out} >0\,\mathrm{h}$ n_{tot} slowly decreases, but less strongly than in W16 liquid origin cirrus. With mean and median values around $0.007\,\mathrm{cm}^{-3}$ n_{tot} is about a factor two larger than in both W16 cirrus categories and almost an order of magnitude larger than in IM in-situ cirrus. This value is consistent ice number concentrations expected for slow-updraft in-situ cirrus from observations and idealized scenarios Krämer et al. (2020). Again by construction f_{liq} is below 0.5 and stays for the majority of the IM in-situ segments between 0 and 0.2 (Figure 8 (l)). Hence, overall microphysical characteristics in the ascent phase resemble those of W16 liquid origin, while there are substantial differences in the outflow phase from both W16 cirrus categories and the IM in-situ cirrus.

Summary

While the two cirrus categories identified with W16 differ substantially in the ascent phase ($t_out <0\,\mathrm{h}$), they have very similar properties in the outflow phase ($t_out >0\,\mathrm{h}$). In contrast, the two cirrus categories classified by our IM based method different more strongly in the outflow phase and somewhat less in the ascent phase. In the ascent phase, q_tot values for both W16 and IM liquid origin cirrus are consistent with those reported for liquid origin cirrus in existing literature; n_{tot} values are lower than reported for liquid origin cirrus. For W16 in-situ cirrus q_{tot} and n_{tot} are also consistent with expectations, but IM in-situ cirrus has substantially larger q_{tot}. 2-4h into the outflow phase, q_{tot} and n_{tot} values for all considered cirrus categories are more consistent with previously reported values for slow-updraft in-situ cirrus than liquid origin cirrus. The results suggest that efficient removal of mixed-phase condensate along with sedimentation of ice formed at (very) low temperatures (DEP/HOM ice modes) is decisive for the microphysical properties of the cirrus in a large fraction WCB outflow parcels.

5 Discussion

The WCB outflow cirrus, i.e. cirrus found in parcels that rise in the WCB core region, is found to be primarily formed by deposition nucleation(DEP). For most WCB outflow cirrus parcels the DEP ice mode accounted for more than $50\,\%$ of the ice

water content. Ice particles initially formed by liquid origin processes are only relevant for fast ascending WCB trajectories. After end of WCB ascent, the contribution of ice from liquid origin processes becomes increasingly more important due to the efficient sedimentation of (large) DEP ice crystals. Hence large parts of the outflow cirrus (in a Eulerian sense) are dominated by ice formed by liquid origin processes, but outflow cirrus are relatively thin with low ice water content and low ice number concentrations.

The ice modes scheme further allows us to revisit the question of what processes control cirrus microphysical properties. To this end we classified WCB outflow cirrus ones according to their thermodynamic history following the classification method proposed by Wernli et al. (2016) (W16 classification) and ones according to the dominant ice particle formation mechanism based on the information from the ice modes scheme (IM based classification). The W16 classification identifies most WCB outflow cirrus segments as liquid origin because they continuously contain ice from the mixed-phase into the cirrus cloud regime. In contrast, the ice modes based classification identifies most trajectories as in-situ origin due to the large fraction of ice water content associated with ice particles formed by deposition nucleation (DEP). These ice particles formed above the main WCB ascent region and sedimented into the ascending air mass. The study by Wernli et al. (2016) demonstrated that for two WCB case studies, the WCB outflow cirrus were embedded in a slow ascending air mass, where ice formed in an in-situ thermodynamic environment. They surmised that at the interface between these two air masses sedimentation could possible 'confuse' the pure thermodynamic cirrus origin classification as it does not take sedimentation into account. The results from our study using the ice modes (IM) scheme confirm that such an interaction between an ascending WCB and enveloping air mass is occurring for the investigated WCB case.

Composite microphysical properties of different cirrus origin classes identified either with the W16 or the IM based classification method are used to investigate the degree to which the sedimenting in-situ ice impacts the properties of thermodynamically liquid-origin cirrus. While liquid and in-situ origin cirrus classified with W16 differ substantially in the ascent phase, they quickly attain similar ice water content and number concentration after the end of the WCB ascent. In contrast, the two cirrus categories identified with the IM based method differ more strongly in the outflow phase, but somewhat less in the ascent phase than those identified by W16.

Hence, we can conclude that sedimentation and a ice formation processes oriented classification is important for vertically deep and complex cloud systems. However, our analysis includes only cirrus formed in WCB trajectories, i.e. strongly ascending parcels. Therefore our results therefore do not discredit the idea of the importance of the thermodynamic history for cirrus properties, but rather suggest that different ice nucleation processes and sedimentational redistribution of ice may modulate cirrus origin and properties. The thermodynamical classification has been proven useful for field campaign planning and interpretation of large data-sets of cirrus observations (e.g. Krämer et al., 2020). It likely remains relevant if looking at a large variety of cirrus clouds in a global perspective. For a detailed investigations of cirrus derived in particular from complex, vertically deep cloud systems as well as for understanding cirrus evolution after first formation, further sub-categories taking into account sedimentation fluxes and ice formation processes in addition to thermodynamic information are needed. This will lead to sharper cirrus property categories, but given our current approach is computationally quite expensive, i.e. not easy to obtain for e.g. flight campaign planning. In future studies we will explore some possibilities of cheaper classification methods that

take into account some of the information on particle sedimentation.

Limitations of the present study should be mentioned here: Generally the ice (formation) processes are not well understood and their representation in numerical models is subject to large uncertainties. In the present study the most important parameter choices are the prescribed distribution of ice nucleating particles (INP) as well as their activation parametrisation. These choices vary widely between commonly used parameterisations of deposition and immersion freezing (e.g. Hawker et al., 2021; Lüttmer et al., 2024). Therefore, we will address the impact of these parameter choices for cirrus properties and their controls in a follow-up study.

Furthermore, the present study focused mainly on the cirrus formed in WCB trajectories, but we also found that ice formed in the more slowly rising air stream surrounding the main WCB ascent is important mainly as a source of ice formed by deposition nucleation. Future studies should consider in more detail the thermodynamic and microphysical evolution of this surrounding cirrus as well as its interaction with the WCB outflow cirrus. It would be also interesting to better understand the horizontal and spatial distribution of the various cirrus types in WCB outflow.

Appendix A: List of abbreviations

Abbreviation	Description
DEP	deposition nucleation ice mode
FRZ	homogeneous freezing of cloud droplets ice mode
HOM	homogeneous freezing of solution droplets ice mode
IM	ice modes based classification
IMM	immersion freezing ice mode
IWC	ice water content
IWP	ice water path
LWC	liquid water content
SEC	secondary ice mode
TOT	sum of all ice modes
W16	thermodynamic based classification (Wernli et al., 2016)
WCB	warm conveyor belt

Table A1. List of abbreviations

Appendix B: Cyclone identification

We developed an algorithm in Python 3 to detect cyclones in pressure fields on a regular grid. An object oriented programming approach lends itself to the identifying of features. The principles are based on the work of Wernli and Schwierz (2006), however we do not include cyclone tracking as we are merely interested in the area where a cyclone is present at any given time. Similar to WS06 the algorithm is based on the analysis of pressure contours and minima. But instead of starting from a (local) minima and consecutively calculating closed contours encapsulating it, we calculate all isobars and filter them by various criteria until we obtain the largest closed contour enclosing a local minima.

The algorithm requires a pressure field and a topography file as input. When identifying a cyclone on surface level it is recommended to use already to mean sea level reduced data, but otherwise there is a (simple) pressure reduction option available in the program. At first minima in the pressure field are detected by simple comparison to its neighbors. The number of adjacent points taken into account depends on the resolution of the grid so that the search range is $5°$. In a limited area mode points near the domain boundary are ignored. For global data a cyclic boundary data mode is available. Values that are unrealistic for a surface level cyclone such as minima below $900\,\mathrm{hPa}$ are discarded. Similar minima that are located $1.5\,\mathrm{km}$ above sea level are filtered out.

Contours are calculated as isobars in $2\,\mathrm{hPa}$ intervals. All non-closed contours are discarded, which limits the applicability of the algorithm in a limited area mode if the cyclone feature of interest is located close to the domain boundary. Especially for

model data with high spatial resolution there will be numerous closed contours that are connected to non-cyclones features like landmasses. So we additionally filter out contours that are to short ($< 200\,\mathrm{km}$) or only enclose a small area ($< 100000\,\mathrm{km}^2$), where for the latter we transform contour coordinates to a sinusoidal equal-area map projection and use Green's theorem for closed curves.

Next the contours are associated with minima that they enclose. Any minima without enclosing contours or contours without associated minima are discarded. The minima are now characterized depending on their distance to each other, their depth and if they share enclosing contours. Minima within the clustering distance ($< 2000\,\mathrm{km}$) and with a shared contour are attributed to the same cyclone with the deepest minima being the primary and the others secondary minima. Contours that enclose multiple minima outside clustering distance are discarded so that they are classified as different cyclones. At last we take the largest contour enclosing a (deepest) minima and label every point within as being inside a cyclone. Note that the values of all selection criterion should be adjusted and tested for the specifics of the chosen dataset. Especially the spatial resolution and smoothness of the surface pressure vary strongly between atmospheric models. The algorithm was tested on ICON data with effective grid resolutions of 7.5 and $13\,\mathrm{km}$ as well as for ERA5 data with a resolution of $0.25°$.

Code availability. The NCL code for the data evaluation is available upon request. The Python code for the cyclone identification algorithm is available upon request.

Data availability. Lagrangian trajectory data will be published upon publication, but can be sent to the reviewers upon request also.

Author contributions. TL, PS and AM designed the study; TL performed the simulations and carried out the data analyses; TL, PS and AM contributed to interpreting the results. TL and AM contributed to writing the paper.

Competing interests. The contact author has declared that none of the authors has any competing interests.

Acknowledgements. The research leading to these results was funded by the German Research Foundation (DFG, Deutsche Forschungsgemeinschaft) through: (1) Transregional Collaborative Research Center SFB/TRR 165 (grant no. 257899354; Waves to Weather) subproject B7 and (2) TRR 301 (grant no. 428312742; The Tropopause Region in a Changing Atmosphere) subproject B08.

Parts of this research were conducted using the supercomputer MOGON 2 and/or advisory services offered by Johannes Gutenberg University Mainz (hpc.uni-mainz.de), which is a member of the AHRP (Alliance for High Performance Computing in Rhineland Palatinate, www.ahrp.info) and the Gauss Alliance e.V.

References

Bechtold, P., Köhler, M., Jung, T., Doblas-Reyes, F., Leutbecher, M., Rodwell, M. J., Vitart, F., and Balsamo, G.: Advances in simulating atmospheric variability with the ECMWF model: From synoptic to decadal time-scales, Quarterly Journal of the Royal Meteorological Society, 134, 1337–1351, https://doi.org/10.1002/qj.289, 2008.

Benas, N., Finkensieper, S., Stengel, M., van Zadelhoff, G.-J., Hanschmann, T., Hollmann, R., and Meirink, J. F.: The MSG-SEVIRI-based cloud property data record CLAAS-2, Earth System Science Data, 9, 415–434, https://doi.org/10.5194/essd-9-415-2017, 2017.

Bigg, E.: The formation of atmospheric ice crystals by the freezing of droplets, Quarterly Journal of the Royal Meteorological Society, 79, 510–519, https://doi.org/10.1002/qj.49707934207, 1953.

Binder, H., Boettcher, M., Joos, H., and Wernli, H.: The Role of Warm Conveyor Belts for the Intensification of Extratropical Cyclones in Northern Hemisphere Winter, Journal of the Atmospheric Sciences, 73, 3997 – 4020, https://doi.org/10.1175/JAS-D-15-0302.1, 2016.

Cotton, R. and Field, P.: Ice nucleation characteristics of an isolated wave cloud, Quarterly Journal of the Royal Meteorological Society: A journal of the atmospheric sciences, applied meteorology and physical oceanography, 128, 2417–2437, https://doi.org/10.1256/qj.01.150, 2002.

Gasparini, B. and Lohmann, U.: Why cirrus cloud seeding cannot substantially cool the planet, Journal of Geophysical Research: Atmospheres, 121, 4877–4893, https://doi.org/10.1002/2015JD024666, 2016.

Gasparini, B., Meyer, A., Neubauer, D., Münch, S., and Lohmann, U.: Cirrus Cloud Properties as Seen by the CALIPSO Satellite and ECHAM-HAM Global Climate Model, Journal of Climate, 31, 1983 – 2003, https://doi.org/10.1175/JCLI-D-16-0608.1, 2018.

Grams, C. M., Wernli, H., Böttcher, M., Čampa, J., Corsmeier, U., Jones, S. C., Keller, J. H., Lenz, C.-J., and Wiegand, L.: The key role of diabatic processes in modifying the upper-tropospheric wave guide: a North Atlantic case-study, Quarterly Journal of the Royal Meteorological Society, 137, 2174–2193, https://doi.org/doi.org/10.1002/qj.891, 2011.

Grams, C. M., Magnusson, L., and Madonna, E.: An atmospheric dynamics perspective on the amplification and propagation of forecast error in numerical weather prediction models: A case study, Quarterly Journal of the Royal Meteorological Society, 144, 2577–2591, https://doi.org/10.1002/qj.3353, 2018.

Gryspeerdt, E., Sourdeval, O., Quaas, J., Delanoë, J., Krämer, M., and Kühne, P.: Ice crystal number concentration estimates from lidar–radar satellite remote sensing – Part 2: Controls on the ice crystal number concentration, Atmospheric Chemistry and Physics, 18, 14 351–14 370, https://doi.org/10.5194/acp-18-14351-2018, 2018.

Hallett, J. and Mossop, S. C.: Production of secondary ice particles during the riming process, Nature, 249, 26–28, https://doi.org/10.1038/249026a0, 1974.

Hande, L. B., Engler, C., Hoose, C., and Tegen, I.: Seasonal variability of Saharan desert dust and ice nucleating particles over Europe, Atmospheric Chemistry and Physics, 15, 4389–4397, https://doi.org/10.5194/acp-15-4389-2015, 2015.

Hawker, R. E., Miltenberger, A. K., Johnson, J. S., Wilkinson, J. M., Hill, A. A., Shipway, B. J., Field, P. R., Murray, B. J., and Carslaw, K. S.: Model emulation to understand the joint effects of ice-nucleating particles and secondary ice production on deep convective anvil cirrus, Atmospheric Chemistry and Physics, 21, 17 315–17 343, https://doi.org/10.5194/acp-21-17315-2021, 2021.

Heinze, R., Dipankar, A., Henken, C. C., Moseley, C., Sourdeval, O., Trömel, S., Xie, X., Adamidis, P., Ament, F., Baars, H., Barthlott, C., Behrendt, A., Blahak, U., Bley, S., Brdar, S., Brueck, M., Crewell, S., Deneke, H., Di Girolamo, P., Evaristo, R., Fischer, J., Frank, C., Friederichs, P., Göcke, T., Gorges, K., Hande, L., Hanke, M., Hansen, A., Hege, H.-C., Hoose, C., Jahns, T., Kalthoff, N., Klocke, D., Kneifel, S., Knippertz, P., Kuhn, A., van Laar, T., Macke, A., Maurer, V., Mayer, B., Meyer, C. I., Muppa, S. K.,

Neggers, R. A. J., Orlandi, E., Pantillon, F., Pospichal, B., Röber, N., Scheck, L., Seifert, A., Seifert, P., Senf, F., Siligam, P., Simmer, C., Steinke, S., Stevens, B., Wapler, K., Weniger, M., Wulfmeyer, V., Zängl, G., Zhang, D., and Quaas, J.: Large-eddy simulations over Germany using ICON: a comprehensive evaluation, Quarterly Journal of the Royal Meteorological Society, 143, 69–100, https://doi.org/https://doi.org/10.1002/qj.2947, 2017.

750 Heise, E., Ritter, B., and Schrodin, R.: Operational implementation of the multilayer soil model, Deutscher Wetterdienst: Offenbach am Main, 2016.

Hong, Y., Liu, G., and Li, J.-L. F.: Assessing the Radiative Effects of Global Ice Clouds Based on CloudSat and CALIPSO Measurements, Journal of Climate, 29, 7651 – 7674, https://doi.org/10.1175/JCLI-D-15-0799.1, 2016.

Huo, J., Tian, Y., Wu, X., Han, C., Liu, B., Bi, Y., Duan, S., and Lyu, D.: Properties of ice cloud over Beijing from surface Ka-band radar
755 observations during 2014–2017, Atmospheric Chemistry and Physics, 20, 14 377–14 392, https://doi.org/10.5194/acp-20-14377-2020, 2020.

Joos, H.: Warm Conveyor Belts and Their Role for Cloud Radiative Forcing in the Extratropical Storm Tracks, Journal of Climate, 32, 5325 – 5343, https://doi.org/10.1175/JCLI-D-18-0802.1, 2019.

Joos, H. and Wernli, H.: Influence of microphysical processes on the potential vorticity development in a warm conveyor belt:
760 a case-study with the limited-area model COSMO, Quarterly Journal of the Royal Meteorological Society, 138, 407–418, https://doi.org/10.1002/qj.934, 2012.

Joos, H., Spichtinger, P., Reutter, P., and Fusina, F.: Influence of heterogeneous freezing on the microphysical and radiative properties of orographic cirrus clouds, Atmospheric Chemistry and Physics, 14, 6835–6852, https://doi.org/10.5194/acp-14-6835-2014, 2014.

Joos, H., Sprenger, M., Binder, H., Beyerle, U., and Wernli, H.: Warm conveyor belts in present-day and future climate simulations – Part 1:
765 Climatology and impacts, Weather and Climate Dynamics, 4, 133–155, https://doi.org/10.5194/wcd-4-133-2023, 2023.

Kärcher, B. and Lohmann, U.: A parameterization of cirrus cloud formation: Homogeneous freezing of supercooled aerosols, Journal of Geophysical Research: Atmospheres, 107, AAC–4, https://doi.org/10.1029/2001JD000470, 2002.

Korolev, A., Heckman, I., Wolde, M., Ackerman, A. S., Fridlind, A. M., Ladino, L. A., Lawson, R. P., Milbrandt, J., and Williams, E.: A new look at the environmental conditions favorable to secondary ice production, Atmospheric Chemistry and Physics, 20, 1391–1429,
770 https://doi.org/10.5194/acp-20-1391-2020, 2020.

Krämer, M., Rolf, C., Luebke, A., Afchine, A., Spelten, N., Costa, A., Meyer, J., Zöger, M., Smith, J., Herman, R. L., Buchholz, B., Ebert, V., Baumgardner, D., Borrmann, S., Klingebiel, M., and Avallone, L.: A microphysics guide to cirrus clouds – Part 1: Cirrus types, Atmospheric Chemistry and Physics, 16, 3463–3483, https://doi.org/10.5194/acp-16-3463-2016, 2016.

Krämer, M., Rolf, C., Spelten, N., Afchine, A., Fahey, D., Jensen, E., Khaykin, S., Kuhn, T., Lawson, P., Lykov, A., Pan, L. L., Riese,
775 M., Rollins, A., Stroh, F., Thornberry, T., Wolf, V., Woods, S., Spichtinger, P., Quaas, J., and Sourdeval, O.: A microphysics guide to cirrus – Part 2: Climatologies of clouds and humidity from observations, Atmospheric Chemistry and Physics, 20, 12 569–12 608, https://doi.org/10.5194/acp-20-12569-2020, 2020.

Lott, F. and Miller, M. J.: A new subgrid-scale orographic drag parametrization: Its formulation and testing, Quarterly Journal of the Royal Meteorological Society, 123, 101–127, 1997.

780 Louis, J.-F.: A parametric model of vertical eddy fluxes in the atmosphere, Boundary-Layer Meteorology, 17, 187–202, 1979.

Luebke, A. E., Afchine, A., Costa, A., Grooss, J.-U., Meyer, J., Rolf, C., Spelten, N., Avallone, L. M., Baumgardner, D., and Kraemer, M.: The origin of midlatitude ice clouds and the resulting influence on their microphysical properties, Atmospheric Chemistry and Physics, 16, 5793–5809, https://doi.org/10.5194/acp-16-5793-2016, 2016.

785 Lüttmer, T., Spichtinger, P., and Seifert, A.: Investigating ice formation pathways using a novel two-moment multi-class cloud microphysics scheme, Accepted for publication, EGUsphere, 2024, 1–36, https://doi.org/10.5194/egusphere-2024-2157, 2024.

Madonna, E., Wernli, H., Joos, H., and Martius, O.: Warm Conveyor Belts in the ERA-Interim Dataset (1979–2010). Part I: Climatology and Potential Vorticity Evolution, Journal of Climate, 27, 3 – 26, https://doi.org/10.1175/JCLI-D-12-00720.1, 2014.

Matus, A. V. and L'Ecuyer, T. S.: The role of cloud phase in Earth's radiation budget, Journal of Geophysical Research: Atmospheres, 122, 2559–2578, https://doi.org/https://doi.org/10.1002/2016JD025951, 2017.

790 Mlawer, E. J., Taubman, S. J., Brown, P. D., Iacono, M. J., and Clough, S. A.: Radiative transfer for inhomogeneous atmospheres: RRTM, a validated correlated-k model for the longwave, Journal of Geophysical Research: Atmospheres, 102, 16 663–16 682, https://doi.org/10.1029/97JD00237, 1997.

Oertel, A., Sprenger, M., Joos, H., Boettcher, M., Konow, H., Hagen, M., and Wernli, H.: Observations and simulation of intense convection embedded in a warm conveyor belt – how ambient vertical wind shear determines the dynamical impact, Weather and Climate Dynamics, 795 2, 89–110, https://doi.org/10.5194/wcd-2-89-2021, 2021.

Oertel, A., Miltenberger, A. K., Grams, C. M., and Hoose, C.: Interaction of microphysics and dynamics in a warm conveyor belt simulated with the ICOsahedral Nonhydrostatic (ICON) model, Atmospheric Chemistry and Physics, 23, 8553–8581, https://doi.org/10.5194/acp-23-8553-2023, 2023.

Orr, A., Bechtold, P., Scinocca, J., Ern, M., and Janiskova, M.: Improved Middle Atmosphere Climate and Forecasts in 800 the ECMWF Model through a Nonorographic Gravity Wave Drag Parameterization, Journal of Climate, 23, 5905 – 5926, https://doi.org/10.1175/2010JCLI3490.1, 2010.

Pfahl, S., Madonna, E., Boettcher, M., Joos, H., and Wernli, H.: Warm Conveyor Belts in the ERA-Interim Dataset (1979–2010). Part II: Moisture Origin and Relevance for Precipitation, Journal of Climate, 27, 27 – 40, https://doi.org/10.1175/JCLI-D-13-00223.1, 2014.

Ramanathan, V., Cess, R. D., Harrison, E. F., Minnis, P., Barkstrom, B. R., Ahmad, E., and Hartmann, D.: Cloud-Radiative Forcing and 805 Climate: Results from the Earth Radiation Budget Experiment, Science, 243, 57–63, https://doi.org/10.1126/science.243.4887.57, 1989.

Raschendorfer, M.: The new turbulence parameterization of LM, COSMO newsletter, 1, 89–97, 2001.

Rasp, S., Selz, T., and Craig, G. C.: Convective and Slantwise Trajectory Ascent in Convection-Permitting Simulations of Midlatitude Cyclones, Monthly Weather Review, 144, 3961 – 3976, https://doi.org/10.1175/MWR-D-16-0112.1, 2016.

Reed, R. J., Stoelinga, M. T., and Kuo, Y.-H.: A Model-aided Study of the Origin and Evolution of the Anomalously High Potential vorticity 810 in the Inner Region of a Rapidly Deepening Marine Cyclone, Monthly Weather Review, 120, 893 – 913, https://doi.org/10.1175/1520-0493(1992)120<0893:AMASOT>2.0.CO;2, 1992.

Rodwell, M., Forbes, R., and Wernli, H.: Why warm conveyor belts matter in NWP, https://doi.org/10.21957/mr20vg, 2018.

Schwenk, C. and Miltenberger, A.: The role of ascent timescale for WCB moisture transport into the UTLS, EGUsphere, 2024, 1–46, https://doi.org/10.5194/egusphere-2024-2402, 2024.

815 Schäfler, A., Craig, G., Wernli, H., Arbogast, P., Doyle, J. D., McTaggart-Cowan, R., Methven, J., Rivière, G., Ament, F., Boettcher, M., Bramberger, M., Cazenave, Q., Cotton, R., Crewell, S., Delanoë, J., Dörnbrack, A., Ehrlich, A., Ewald, F., Fix, A., Grams, C. M., Gray, S. L., Grob, H., Groß, S., Hagen, M., Harvey, B., Hirsch, L., Jacob, M., Kölling, T., Konow, H., Lemmerz, C., Lux, O., Magnusson, L., Mayer, B., Mech, M., Moore, R., Pelon, J., Quinting, J., Rahm, S., Rapp, M., Rautenhaus, M., Reitebuch, O., Reynolds, C. A., Sodemann, H., Spengler, T., Vaughan, G., Wendisch, M., Wirth, M., Witschas, B., Wolf, K., and Zinner, T.: The North Atlantic Waveguide and 820 Downstream Impact Experiment, Bulletin of the American Meteorological Society, 99, 1607 – 1637, https://doi.org/10.1175/BAMS-D-17-0003.1, 2018.

Seidel, J. S., Kiselev, A. A., Keinert, A., Stratmann, F., Leisner, T., and Hartmann, S.: Secondary ice production – no evidence of efficient rime-splintering mechanism, Atmospheric Chemistry and Physics, 24, 5247–5263, https://doi.org/10.5194/acp-24-5247-2024, 2024.

Seifert, A. and Beheng, K. D.: A two-moment cloud microphysics parameterization for mixed-phase clouds. Part 1: Model description, Meteorology and atmospheric physics, 92, 45–66, https://doi.org/10.1007/s00703-005-0112-4, 2006.

Sourdeval, O., Gryspeerdt, E., Krämer, M., Goren, T., Delanoë, J., Afchine, A., Hemmer, F., and Quaas, J.: Ice crystal number concentration estimates from lidar–radar satellite remote sensing – Part 1: Method and evaluation, Atmospheric Chemistry and Physics, 18, 14 327–14 350, https://doi.org/10.5194/acp-18-14327-2018, 2018.

Spichtinger, P. and Gierens, K. M.: Modelling of cirrus clouds – Part 1a: Model description and validation, Atmospheric Chemistry and Physics, https://doi.org/10.5194/acp-9-685-2009, 2009.

Spreitzer, E., Attinger, R., Boettcher, M., Forbes, R., Wernli, H., and Joos, H.: Modification of potential vorticity near the tropopause by nonconservative processes in the ECMWF model, Journal of the Atmospheric Sciences, 76, 1709–1726, https://doi.org/10.1175/JAS-D-18-0295.1, 2019.

Sprenger, M. and Wernli, H.: The LAGRANTO Lagrangian analysis tool – version 2.0, Geoscientific Model Development, 8, 2569–2586, https://doi.org/10.5194/gmd-8-2569-2015, 2015.

Stephens, G. L.: Radiation Profiles in Extended Water Clouds. II: Parameterization Schemes, Journal of Atmospheric Sciences, 35, 2123 – 2132, https://doi.org/10.1175/1520-0469(1978)035<2123:RPIEWC>2.0.CO;2, 1978.

Urbanek, B., Groß, S., Schäfler, A., and Wirth, M.: Determining stages of cirrus evolution: a cloud classification scheme, Atmospheric Measurement Techniques, 10, 1653–1664, https://doi.org/10.5194/amt-10-1653-2017, 2017.

Vali, G., DeMott, P. J., Möhler, O., and Whale, T. F.: Technical Note: A proposal for ice nucleation terminology, Atmospheric Chemistry and Physics, 15, 10 263–10 270, https://doi.org/10.5194/acp-15-10263-2015, 2015.

Wernli, H. and Gray, S. L.: The importance of diabatic processes for the dynamics of synoptic-scale extratropical weather systems – a review, Weather and Climate Dynamics, 5, 1299–1408, https://doi.org/10.5194/wcd-5-1299-2024, 2024.

Wernli, H. and Schwierz, C.: Surface Cyclones in the ERA-40 Dataset (1958–2001). Part I: Novel Identification Method and Global Climatology, Journal of the Atmospheric Sciences, 63, 2486 – 2507, https://doi.org/10.1175/JAS3766.1, 2006.

Wernli, H., Boettcher, M., Joos, H., Miltenberger, A. K., and Spichtinger, P.: A trajectory-based classification of ERA-Interim ice clouds in the region of the North Atlantic storm track, Geophysical Research Letters, 43, 6657–6664, https://doi.org/10.1002/2016GL068922, 2016.

Wolf, V., Kuhn, T., Milz, M., Voelger, P., Krämer, M., and Rolf, C.: Arctic ice clouds over northern Sweden: microphysical properties studied with the Balloon-borne Ice Cloud particle Imager B-ICI, Atmospheric Chemistry and Physics, 18, 17 371–17 386, https://doi.org/10.5194/acp-18-17371-2018, 2018.

Zhang, Y., Macke, A., and Albers, F.: Effect of crystal size spectrum and crystal shape on stratiform cirrus radiative forcing, Atmospheric Research, 52, 59–75, https://doi.org/https://doi.org/10.1016/S0169-8095(99)00026-5, 1999.